Environmental Science & Technology

Article

Cite This: Environ. Sci. Technol. 2019, 53, 13495−13505

pubs.acs.org/est

Novel Insights into the Kinetics, Evolved Gases, and Mechanisms for Biomass (Sugar Cane Residue) Pyrolysis

Fanhao Song,[‡,†] Tingting Li,[‡] Jin Zhang,[‡] Xiaojie Wang,[§] Yingchen Bai,[*,‡] John P. Giesy,[‡,⊥] Baoshan Xing,[∥] and Fengchang Wu[‡]

[‡]State Key Laboratory of Environmental Criteria and Risk Assessment, Chinese Research Academy of Environmental Sciences, Beijing, 10012, China

[†]College of Water Sciences, Beijing Normal University, Beijing 100875, China

[§]Guangzhou Institute of Geochemistry, Chinese Academy of Sciences, Guangzhou 510640, China

[⊥]Department of Biomedical and Veterinary Biosciences and Toxicology Centre, University of Saskatchewan, Saskatoon, Saskatchewan, SK S7N 5B3, Canada

[∥]Stockbridge School of Agriculture, University of Massachusetts, Amherst, Massachusetts 01003, United States

Supporting Information

ABSTRACT: Biomass, a renewable energy source, via available thermo-chemical processes has both engineering and environmental advantages. However, the understanding of the kinetics, evolved gases, and mechanisms for biomass pyrolysis is limited. We first propose a novel temperature response mechanism for the pyrolysis of sugar cane residue using thermogravimetric analysis-Fourier transform infrared spectrometry-mass spectrometry (TG-FTIR-MS) combined with Gaussian model and two-dimensional correlation spectroscopy (2D COS). The existence and contribution of distinct peaks in TG-FTIR spectra were innovatively distinguished and quantified, and the temperature-dependent dynamics of gas amounts were determined using Gaussian deconvolution. The 2D-TG-FTIR/MS-COS results revealed for the first time that the primary sequential temperature responses of gases occurred in the order: H_2O/CH_4 > phenols/alkanes/aromatics/alcohols > carboxylic acids/ketones > CO_2/ethers > aldehyde groups/acetaldehyde. Subtle sequential changes even occurred within the same gases during pyrolysis. The quantity dynamics and sequential responses of gases were fitted to the combined effects of the order-based, diffusion, and chemical reaction mechanisms for the component degradation. The combination of TG-FTIR-MS, Gaussian model, and 2D COS is a promising approach for the online monitoring and real-time management of biomass pyrolysis, providing favorable strategies for pyrolysis optimization, byproduct recovery, energy generation, and gas emission control in engineering and environmental applications.

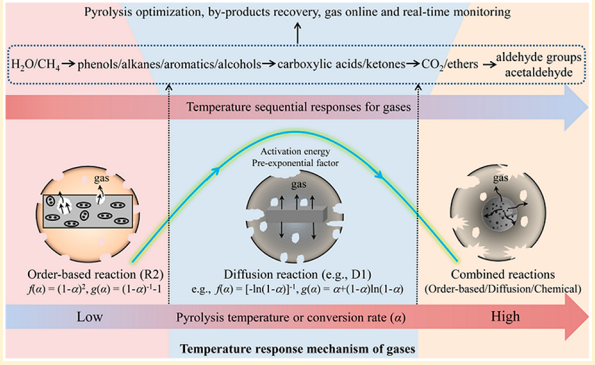

INTRODUCTION

The development and utilization of biomass, a renewable and sustainable energy source, have attracted significant attention due to its potential for producing energy products and reducing release risk of environmental pollution.[1−4] Biomass has been reported to provide approximately 1250 million tons of crude oil equivalents of primary energy, accounting for approximately 14% of annual energy consumption globally.[5] Sugar cane residue (SCR) is one of the important biomass feedstocks in China, due to its large-scale production. The effective use of SCR can significantly reduce carbon emissions compared with fossil fuels.[6] Moreover, SCR-derived biochar has the potential as a soil amendment to increase soil fertility and organic carbon sequestration.[7,8] Therefore, the environmental and engineering applications of SCR are of interest, and these applications are primarily affected by its thermal conversion, pyrolysis kinetic, and thermodynamic properties.

The efficiency and productivity of the biomass pyrolysis reactions are regulated by many factors, such as the heating rate, residence time, and reactants.[9,10] For example, increasing heating rates can increase the temperature range of the devolatilization stage, causing differences in weight losses and releasing gases during biomass pyrolysis.[11] Additionally, the heating rate also significantly affects biomass carbonization, which results in solid products (e.g., biochar) with a wide range of functional and structural properties.[9,11] Despite the

Received: July 30, 2019
Revised: October 3, 2019
Accepted: October 23, 2019
Published: October 23, 2019

DOI: 10.1021/acs.est.9b04595
Environ. Sci. Technol. 2019, 53, 13495−13505

massive use of SCR in terms of pyrolysis applications, the effects of heating rates on its thermal behaviors are still poorly understood. Furthermore, the knowledge of SCR pyrolysis mechanisms is imperative for optimizing reaction parameters and balancing mass and energy.[12] The pyrolysis mechanisms of individual components in SCR are very complex and heterogeneous because the components are chemically different from species to species.[13,14] Previous studies have established thermodynamic parameters to study the solid-state reaction mechanisms of biomass pyrolysis using integral methods, such as the Flynn-Wall-Ozawa (FWO) method and the distributed activation energy model (DAEM).[1,15] However, the combined mechanisms of heterogeneous solid−gas reactions at the molecular level of biomass (i.e., SCR) pyrolysis under different heating rates are still unclear due to the complex reactions of the pyrolysis process.

The evaluation of pyrolysis gases is useful in providing theoretical support for the recovery of byproducts, the cycle of atmospheric carbon, and the control of greenhouse gas emissions in the future. Thermogravimetric analysis combined with Fourier transform infrared spectrometry and mass spectrometry (TG-FTIR-MS) can corroborate the result validity by comparing the respective thermograms and spectrograms of the evolved gaseous species.[16] By reducing the interference caused by similar absorption bands and mass-to-charge ratios (m/z), TG-FTIR-MS analysis is a potential method for the nondestructive, simultaneous, real-time measurement of multiple gaseous species in complex mixtures resulting from biomass pyrolysis.[16,17] However, TG-FTIR analysis suffers from a limitation with respect to effectively quantifying the volatile gaseous species from biomass pyrolysis. Moreover, the peaks in the TG-FTIR spectra are generally rather broad and featureless because the peaks in such complex multicomponent systems usually overlap.[18,19] It is necessary to use a model to perform the spectral decomposition, peak fitting, and quantification of the TG-FTIR spectra. The Gaussian model has proven to be an efficient method to distinguish the overlaps and reveal "hidden" peaks during spectroscopic analyses.[18,19] Furthermore, the contribution of each separated peak to the integral spectrum can be calculated to quantify the amounts of individual components or functional groups.[18] Previous studies have characterized both functional and structural properties of energy feedstocks (e.g., lignites) using normal FTIR coupled with a Gaussian model.[19] However, no studies have been performed to quantitatively investigate the thermal characteristics and evolved gases of biomass (i.e., SCR) pyrolysis using TG-FTIR combined with Gaussian model.

Without careful interpretation and model analysis of the TG-FTIR-MS spectra, it is also difficult to effectively investigate the temperature-dependent dynamics of the primary gases resulting from biomass pyrolysis. Two-dimensional correlation spectroscopy (2D COS) is a powerful approach to thoroughly analyze the various spectral data measured under the influence of external perturbations.[20,21] The 2D COS can sort out subtle key information from the spectral signal variations from a single spectral probe in a specific system, which can be hidden or hardly detected in a conventional one-dimensional spectrum (e.g., TG-FTIR and TG-MS).[21,22] The 2D COS is useful for simplifying complex spectra consisting of many overlapping peaks and enhancing the spectral resolution by extending the spectra along the second dimension.[23,24] In addition, 2D COS also has the advantages of establishing clear assignments using band correlations and identifying the order of subtle spectral changes in response to external perturbations.[25,26] In fact, various kinds of probes exist to reflect the specific aspects of a specific system.[23] Hetero 2D COS is a derived 2D correlation analysis that can provide complementary and comprehensive information regarding the corrections and underlying relationships among signals in two types of probes.[23] Previous studies have utilized traditional FTIR combined with 2D COS to investigate subtle variations, change directions, and the sequential order of fluorescent components in organic matter caused by external perturbation.[20] However, to the best of our knowledge, this is the first time that 2D COS and hetero 2D COS analyses are used to study the subtle and sequential temperature responses of gas products from biomass (i.e., SCR) pyrolysis based on TG-FTIR-MS data.

The primary objective of this study is to further elucidate the kinetics, evolved gases, and reaction mechanisms that occur during biomass pyrolysis. For this purpose, SCR was taken as an example and its pyrolysis characteristics of kinetics, pseudocomponents, and solid-state reaction mechanisms under different heating rates were evaluated using TG combined with integral methods and Gaussian model. The accurate identification, differentiation, and quantification of gaseous species from SCR pyrolysis were performed using Gaussian deconvolution with TG-FTIR spectra. Furthermore, the subtle variations, directions, and sequential temperature responses of gaseous species from SCR pyrolysis were evaluated using novel 2D-TG-FTIR/MS-COS analysis for the first time. Finally, a novel temperature-response mechanism at the molecular level was established to connect the solid-state reaction mechanisms with the gas sequential responses for biomass pyrolysis.

MATERIALS AND METHODS

Sample Preparation, TG-FTIR-MS Analysis and Integral Methods. Detailed information for the preparation, characterization, and TG-FTIR-MS analysis of SCR can be obtained in the Supporting Information section (SI, Figure S1, Table S1). The kinetic and thermodynamic parameters of SCR pyrolysis were determined using the FWO and DAEM methods (eqs 1 and 2) based on the TG and derivative TG (DTG) data (SI).[15]

$$\ln(\beta) = \ln\left(\frac{A\cdot Ea}{R\cdot G(\alpha)}\right) - \frac{Ea}{RT} \tag{1}$$

$$\ln\left(\frac{\beta}{T^2}\right) = \ln\frac{AR}{Ea} + 0.6075 - \frac{Ea}{RT} \tag{2}$$

where β and R represent the constant heating rate and universal gas constant (R = 8.3145 J·mol^{-1}·K^{-1}), respectively. At a conversion rate (α) range of 0.2−0.8 with an interval of 0.05, both the activation energy (Ea) and pre-exponential factor (A) values were determined using the FWO and DAEM methods from the linear plots of $\log(\beta)$ and $\ln\left(\frac{\beta}{T^2}\right)$ versus $1/T$, respectively. The thermodynamic parameters, including the changes in enthalpy (ΔH), Gibb's free energy (ΔG), and entropy (ΔS) were also calculated (SI).[27,28]

Criado Method. The Criado method has been widely used to determine the kinetic mechanisms of the solid-state reactions of biomass pyrolysis.[29,30] The Z-master plots

DOI: 10.1021/acs.est.9b04595
Environ. Sci. Technol. 2019, 53, 13495−13505

($Z(\alpha)$) derived from the Criado method for pyrolysis are described using a mathematical relationship (Table S2, eq 3).[29,30]

$$\frac{Z(\alpha)}{Z(0.5)} = \frac{f(\alpha) \times g(\alpha)}{f(0.5) \times g(0.5)} = \left(\frac{T_\alpha}{T_{0.5}}\right)^2 \times \frac{\left(\frac{d\alpha}{dt}\right)_\alpha}{\left(\frac{d\alpha}{dt}\right)_{0.5}} \quad (3)$$

where $f(\alpha)$ and $g(\alpha)$ represent the physical models designed using different assumptions, and T_α is the pyrolysis temperature at α. The considered kinetic mechanisms have standard master plots that intersect each other corresponding to the $\frac{Z(\alpha)}{Z(0.5)}$ value of 1.

Gaussian Model for the DTG and TG-FTIR Spectra. The Gaussian model was processed to determine the existence and contributions of distinct peaks in the DTG and TG-FTIR spectra, which represented the components in the SCR and gas products from pyrolysis (SI). It is assumed that the experimental spectrum $E_{exp}(x)$ at a spectral variable (x) is superimposed by a single characteristic peak $S_i(x)$ ($i = 1, 2, \ldots, n$).[31] The relationship between $E_{exp}(x)$ and $S_i(x)$ can be expressed as eq 4

$$E_{exp}(x) = \sum S_i(x) \quad (4)$$

The Gauss-Lorentz amplitude function is used to simulate each of the characteristic peaks (eq 5).

$$S_i(x) = a_3 G_i(x) + (1 - a_3) L_i(x) \quad (5)$$

The Gauss and Lorentz amplitude expressions are then expressed as $G_i(x)$ and $L_i(x)$ using eqs 6 and 7, respectively.

$$Gi(x) = a_{0i} \exp\left[-\frac{(x - a_{1i})^2}{2a_{2i}^2}\right] \quad (6)$$

$$L_i(x) = \frac{a_{0i}}{1 + \left[\frac{(x - a_{1i})}{a_{2i}}\right]^2} \quad (7)$$

On the basis of the DTG fitted peak and its area (A_i) of the constituent component, the weight loss rate (r_i) at the fitted peak temperature (T_p) and the contribution of the partial process of the constituent component to the overall mass loss (C_i) were first defined to elucidate the degradation of hemicellulose, cellulose, and lignin in the SCR (eq 8).

$$r_i = \frac{d\alpha}{dT_p}; \qquad C_i = (\alpha_{T_1} - \alpha_{T_2})A_i = \left(\frac{m_{T_0} - m_{T_1}}{m_{T_0} - m_{T_2}}\right)A_i \quad (8)$$

where α_{T_1} and α_{T_2} are the conversion rates at temperatures of T_1 (100 °C) and T_2 (800 °C), respectively. The m_{T_1} and m_{T_2} represent the actual masses at T_1 and T_2, respectively.

The 2D Correlation Spectroscopy for the TG-FTIR-MS Spectra. On the basis of the spectral data, the 2D COS analysis can generate synchronous and asynchronous maps by extending the one-dimensional forms of the variations into two-dimensional domains (SI, Figure S2).[21,32,33] As a function of a spectral variable (x) and an external variable (t), the relationship between spectral changes of $y(x, t)$ and dynamic spectra $\tilde{y}(x,t)$ can be given as eq 9.[20−22]

$$\tilde{y}(x, t) = \begin{cases} y(x, t) - \bar{y}(x) & \text{for } t_{min} \le t \le t_{max} \\ 0 & \text{otherwise} \end{cases} \quad (9)$$

where $\bar{y}(x) = \frac{1}{t_{max} - t_{min}} \int_{t_{min}}^{t_{max}} y(x, t)dt$ is the reference spectrum, denoting the t variable stationary or the averaged spectrum. The 2D synchronous spectrum is given as eq 10

$$\varphi(x_1, x) = \frac{1}{t_{max} - t_{min}} \int_t^{t_{max}} \tilde{y}(x_1, t)\tilde{\tilde{y}}(x_2, t)dt \quad (10)$$

On the basis of the cross-correlation of the dynamic spectrum and the Hilbert-transformed orthogonal spectrum $\tilde{z}(x_2,t)$, the 2D asynchronous spectrum can be represented as eq 11

$$\Psi(x_1, x_2) = \frac{1}{t_{max} - t_{min}} \int_t^{t_{max}} \tilde{y}(x_1, t) \cdot \tilde{z}(x_2, t)dt \quad (11)$$

In this study, the 2D COS was performed using 2D-Shige software developed by Kwansei Gakuin University (Tokyo, Japan). Eleven non-negative TG-FTIR spectra with temperatures in 50 °C unit increments from 50 to 650 °C were selected for the 2D COS analysis. On the basis of the selected data from the TG-FTIR and the TG-MS analyses, hetero 2D COS was also complementarily used to study the sequential responses of gases to the pyrolysis temperature during the SCR pyrolysis process (Figure S2).

RESULTS AND DISCUSSION

Thermodynamic and Kinetic Characteristics. The SCR weight losses in the TG and DTG curves were primarily associated with the evaporation of water and the degradation of hemicellulose, cellulose, and lignin/fixed carbon (Figure S3b).[11,34,35] The shifts of shoulders or peaks in the TG and DTG curves to a higher heating rate were primarily attributed to the heat and mass transfer limitations (Figure S3b).[1] With the Gaussian deconvolution of the differential thermal analysis (DTA) curve at 10 °C·min^{-1} (Figure S3c), the endothermic reaction was associated with moisture release, while the exothermic reaction was related to dehydration, decarboxylation, and decomposition of components in the SCR.[36] The Gaussian peak area for the first (245 °C) exothermic reaction (124.01 μV·mg^{-1}) was higher than that for the second (376 °C) exothermic reaction (94.74 μV·mg^{-1}) (Figure S3d). This result suggested that the decarboxylation of acidic groups, proteins, carbohydrates, and fatty acids in the SCR was stronger than the reaction of aromatic structure breakage and C−C bond cleavage during the pyrolysis process.[36] On the basis of the Arrhenius function, the FWO and DAEM derived curve-fitting plots at four heating rates had strong linear relationships (R^2 = 0.9600−0.9971) (Figure S4, Table S3). The *Ea* and *A* values from both the FWO and DAEM methods at various α values varied in the range of 199.49−272.12 kJ·mol^{-1} and 2.67 × 10^{12}−5.45 × 10^{20} s^{-1}, respectively (Table S3). The α-dependent trends of the *Ea* values from the FWO and DAEM methods showed excellent agreement with each other, which validated the accuracy and reliability of the *Ea* values for SCR pyrolysis (Figure S5a).[34] As a function of increasing α values, significant fluctuations of the *Ea* values and greater *A* values ($A \ge 10^9$ s^{-1}) revealed the complex reactions of the SCR pyrolysis process (Figure S5a, Table S3).[37,38] The increases, decreases, and fluctuations of the *Ea* values at different α ranges were attributed to the thermal degradations

DOI: 10.1021/acs.est.9b04595
Environ. Sci. Technol. 2019, 53, 13495−13505

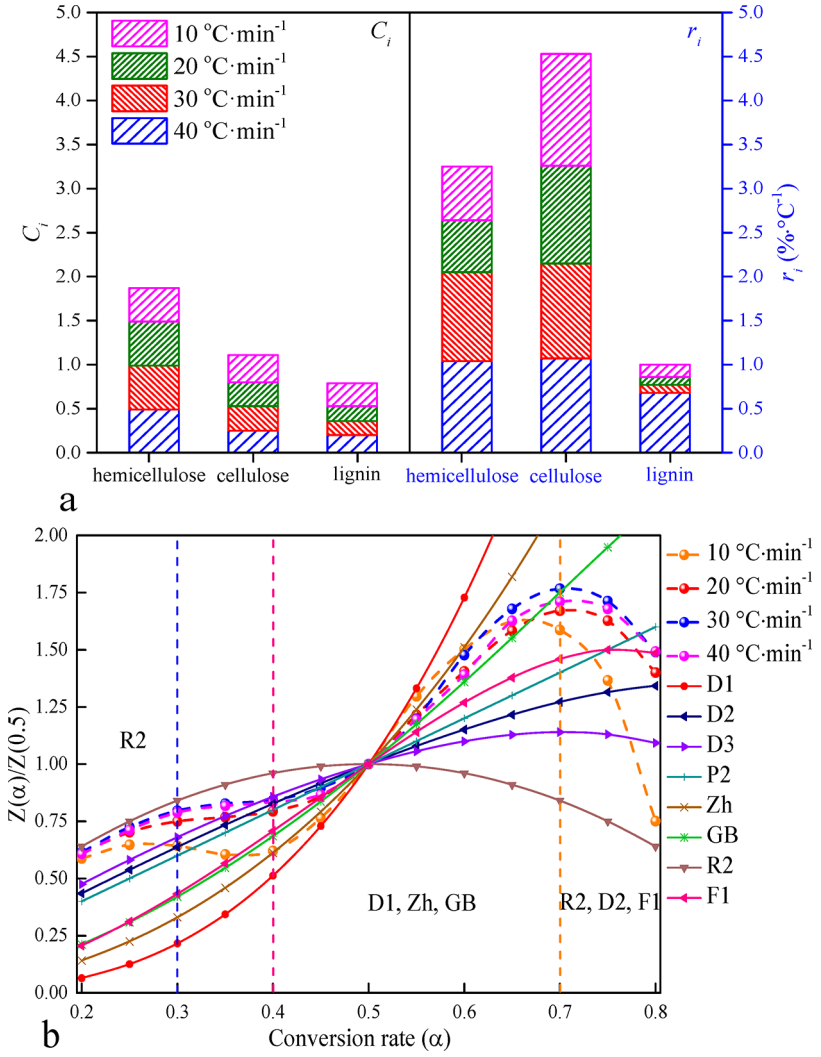

Figure 1. Optimized decomposition parameters (a) and theoretical and experimental plots (b) for determination of SCR pyrolysis mechanisms.

of various components, such as the cross-linked polymer matrix and active cellulose (SI, Figure S5a).[28,39,40] The ΔH values calculated from both the FWO and DAEM methods ranged 194.16−266.88 kJ·mol^{-1} (Table S3). The ΔH values showed exactly the same α-dependent trends as the *Ea* values (Figure S5a,b), suggesting that the activated complex formations for the conversion of reactants to products were easier.[41] The positive ΔG values with a range of 153.90−220.64 kJ·mol^{-1} indicated that the unfavorable reactions that required significant energy input occurred in the SCR pyrolysis system (Figure S5c, Table S3).[28,30] In addition, the almost positive ΔS values suggested that the SCR pyrolysis system might be far from thermal equilibrium (Table S3).[30] The appearance of several negative ΔS values might be associated with the manifestation of complex and disordered reactions during the conversion of SCR into various products (Table S3).[30] Detailed information regarding the thermodynamic and kinetic characteristics of the SCR pyrolysis is given in the Supporting Information section.

Evaluation of Pseudocomponents and Solid-state Reaction Mechanisms. A new attempt and application of DTG combined with Gaussian model was conducted to construct a more comprehensive picture of the complex kinetic characteristics of the pseudocomponents in the SCR. The optimized decomposition processes of the pseudocomponents were determined using the Gaussian model at four heating rates (R^2 = 0.9917−0.9979) (Figure S6). The fitted pseudocomponents of hemicellulose, cellulose, and lignin exhibited similar temperature ranges as the results of the DTG analysis (Figures S3b and S6). Interestingly, the DTG curves at 30 and 40 °C·min^{-1} exhibited two peaks for the hemicellulose pseudocomponent, showing better modeling using four independent reactions (Figure S6c,d). The best fitted model parameters for the pseudocomponents are summarized in Figure 1a and Table S4. The T_p values of pseudocomponents reached the maximum value at relatively higher heating rates (i.e., 30 or 40 °C·min^{-1}) (Table S4), which was mainly attributed to uneven heating and heat transfer limitations.[1] More succinctly, the temperature gradients occurred between the outside surface and the inner core of the SCR particle, and the higher heating rates caused a higher heat transfer limitation for SCR pyrolysis.[42] The C_i values of pseudocomponents at each heating rate followed the order: hemicellulose > cellulose > lignin (Figure 1a, Table S4), indicating that hemicellulose and lignin had the largest and lowest individual contributions to the total decomposition rate, respectively. This result was associated with the different molecular structures and thermal stabilities among the

DOI: 10.1021/acs.est.9b04595
Environ. Sci. Technol. 2019, 53, 13495−13505

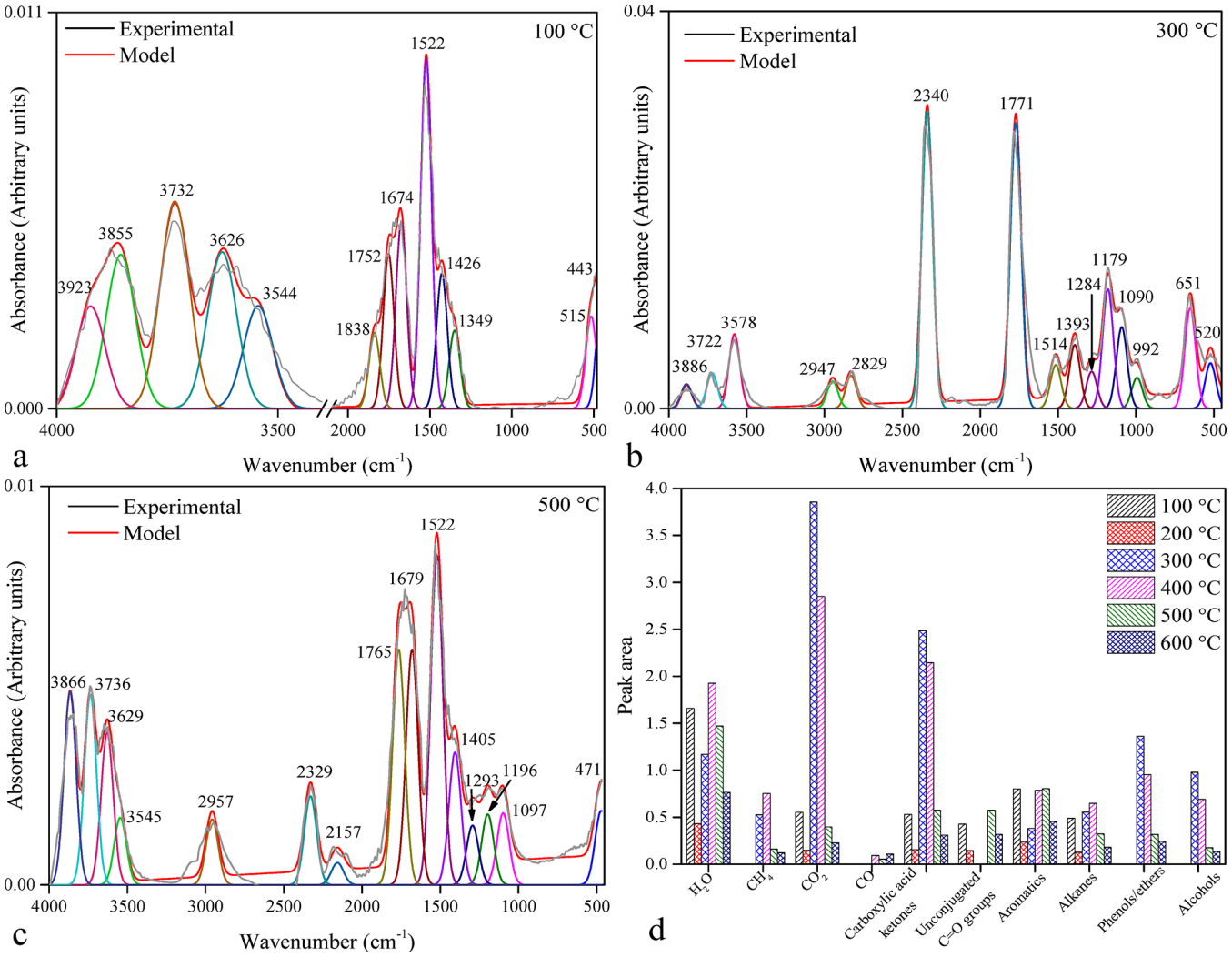

Figure 2. Curve fitting of selected TG-FTIR spectra (a–c) and temperature-dependent Gaussian peak areas for various gases (d).

pseudocomponents in the SCR. Compared to hemicellulose and cellulose, lignin contains abundant aromatic rings with strong cross-linked properties, which are difficult to decompose.[11] In addition, hemicellulose exhibited the lowest decomposition contribution rate at a heating rate of 10 °C·min^{-1}, while cellulose and lignin had the largest contribution rates (Figure 1a, Table S4). Therefore, the heating rates affected the decomposition contribution rates of the pseudocomponents in the SCR. In detail, the lower the heating rate, the larger the decomposition contribution rate for pseudocomponents with higher thermal stability. The r_i values of cellulose at the four heating rates were larger than those of hemicellulose and lignin (Figure 1a, Table S4), indicating greater rates of mass loss at peak temperatures for cellulose in the SCR. Moreover, the largest rates of mass loss at the peak temperature appeared for cellulose at 10 °C·min^{-1} and for hemicellulose and lignin at 40 °C·min^{-1} (Figure 1a, Table S4). This result suggested that the mass loss of cellulose in the SCR was affected to a higher degree by the lower heating rates than those of hemicellulose and lignin. Therefore, the DTG-Gaussian model is a simple form and good prediction to simulate the thermal degradation process of pseudocomponents in biomass.

The predominant solid-state reaction mechanisms as a function of the α value for SCR pyrolysis were determined by theoretical master plots using the Criado method (Figure 1b, Table S2). The experimental plots of the SCR pyrolysis varied with different heating and conversion rates, indicating that each stage of pyrolysis could not be described using a single kinetic model (Figure 1b). The α-dependent trends of $Z(\alpha)/Z(0.5)$ at 20–40 °C·min^{-1} showed excellent agreement with each other, while the trends of $Z(\alpha)/Z(0.5)$ at 10 °C·min^{-1} were more sensitive to change with α values (Figure 1b). The degradation profiles at 20–40 °C·min^{-1} (α = 0.20–0.30) had the closest match with the R2 theoretical plot ($f(\alpha) = (1-\alpha)^2$; $g(\alpha) = (1-\alpha)^{-1} - 1$), which corresponded to the second order random nucleation with two nuclei on an individual particle for the order-based reaction (Figure 1b, Table S2).[30] However, the degradation profiles at 10 °C·min^{-1} (α = 0.20–0.40) and 20–40 °C·min^{-1} (α = 0.30–0.40) crossed the multiple theoretical master plots with poor fitting results (Figure 1b), indicating the transition for multiple and complex reaction mechanisms at these regions. The degradation profiles at 10 °C·min^{-1} (α = 0.40–0.55) were more inclined to the D1 theoretical plot ($f(\alpha) = (1/2)\alpha$; $g(\alpha) = \alpha^2$) that corresponded to the one way transport for the diffusion reaction (Figure 1b, Table S2).[30] In addition, the degradation profiles at 20–40 °C·

DOI: 10.1021/acs.est.9b04595
Environ. Sci. Technol. 2019, 53, 13495–13505

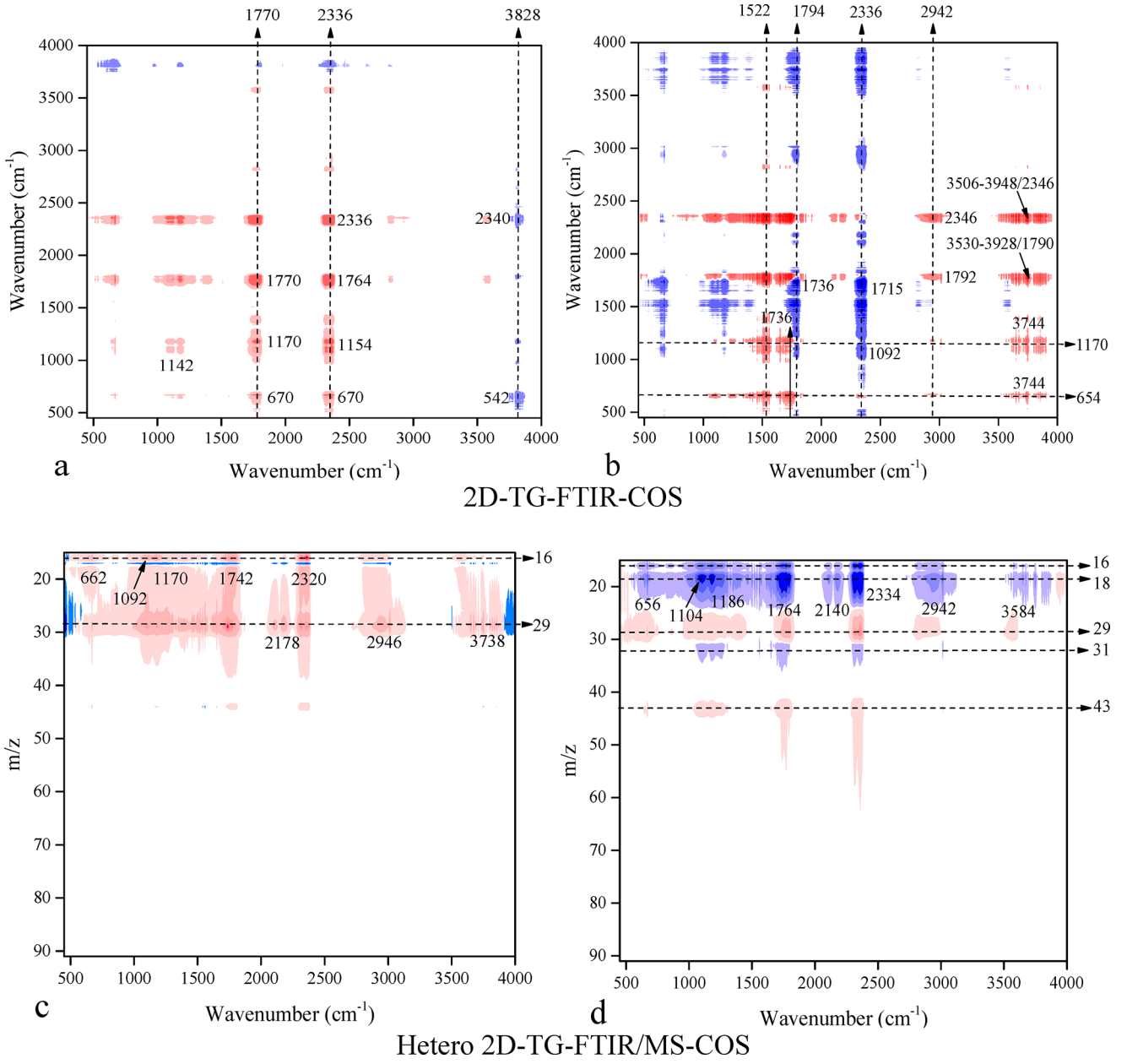

Figure 3. Synchronous (a) and asynchronous (b) maps of the 2D COS and heterosynchronous (c) and heteroasynchronous (d) maps of the hetero 2D COS according to TG-FTIR-MS data of gases with increasing pyrolysis temperatures. The red and blue colors represent the positive and negative correlations for the peaks at $v1/v2$ (x/y axis), respectively. More intense colors indicate stronger positive or negative correlations.

min^{-1} (α = 0.40−0.55) were mainly close to the theoretical plots of the Zhravlev equation (Zh) ($f(\alpha) = (2/3)(1-\alpha)^{5/3}/[1-(1-\alpha)^{1/3}]$; $g(\alpha) = [(1-\alpha)^{-1/3}-1]^2$) and the Ginstling-Brounshtein equation (GB) ($f(\alpha) = (2/3)(1-\alpha)^{1/3}/[1-(1-\alpha)^{1/3}]$; $g(\alpha) = 1-2\alpha/3-(1-\alpha)^{2/3}$) for the diffusion reaction (Figure 1b, Table S2).[30,43] At an α range of 0.55−0.70, the degradation profiles at four heating rates were nearly between the theoretical plots of the Zh and GB equations (Figure 1b). At an α range of 0.70−0.80, the $Z(\alpha)/Z(0.5)$ at four heating rates decreased sharply with increasing α values and poorly fitted the theoretical models (Figure 1b), showing complex reaction mechanisms. At the end α value of 0.80, the degradation profiles at 10 °C·min^{-1} and 20−40 °C·min^{-1} had the closest match with the R2 and D2/F1 theoretical plots, respectively (Figure 1b). The D2 and F1 mechanisms corresponded to the two way transport (Valensi model) ($f(\alpha) = [-\ln(1-\alpha)]^{-1}$; $g(\alpha) = \alpha + (1-\alpha)\ln(1-\alpha)$) for the diffusion reaction and the Sigmoidal rate equations (Prout-Tomkins) ($f(\alpha) = \alpha(1-\alpha)$; $g(\alpha) = -\ln(1-\alpha)$) for the chemical reaction, respectively (Table S2).[12,30] Therefore, the mechanisms of SCR pyrolysis were quite complex and were possibly rendered as the combined effects of the order-based reactions, the diffusion reactions, and the chemical reactions.

Releasing Characteristics and the Quantification of Gas Products. The releasing characteristics of volatile gaseous species from SCR pyrolysis determined using the TG-FTIR-MS are summarized and discussed in detail in the Supporting Information section (Figure S7, Tables S5 and S6). Unfortunately, the online in situ TG-FTIR analysis could not identify and quantify either the highly overlapped peaks in the spectra or the contents of the specific gaseous species; therefore, data interpretation using the Gaussian model was

DOI: 10.1021/acs.est.9b04595
Environ. Sci. Technol. 2019, 53, 13495−13505

needed. Except for the strong peaks in the TG-FTIR spectra, several weak or hidden peaks for gases were also distinguished and quantified using the Gaussian model, such as CO (C−O stretching), unconjugated C=O groups (C=O stretching), phenols, ethers (C−O and O−H stretching), and alcohols (C−O and O−H stretching) (Figures 2 and S8, Table S5).[34,44] The parameters from the Gaussian deconvolution of the TG-FTIR spectra at selected temperatures were distinguished and calculated (Figures 2 and S8).[1,44−47] The larger peak areas of CO_2, H_2O, carboxylic acids, and ketones at selected temperatures indicated their dominance in the volatile components (Figure 2d). The amounts of CO_2, H_2O, carboxylic acids and ketones produced at 100 °C were greater than their amounts released at 200 °C (Figure 2d), which was associated with water evaporation and volatile releases from the SCR particle pores.[48] Additionally, the amounts of CO_2, carboxylic acids and ketones increased rapidly in a temperature range of 200−300 °C and decreased significantly at greater than 400 °C (Figure 2d). In general, the greater releases of CO_2 at medium temperatures were related to the breaking and reforming of lateral chains in the lignin polymer and the thermolabile functional groups in the SCR, such as aliphatic hydroxyl, carboxyl, and carbonyl groups.[47] The higher yields of carboxylic acids and ketones indicated a relatively high content of cellulose in the SCR, as well as a high degree of dehydration, fragmentation, and retroaldol condensation for anhydro-sugars from depolymerization during the pyrolysis process.[49,50] Moreover, the temperature-dependent amounts of aromatics and alkanes changed in a similar manner to the amounts of CO_2, H_2O, carboxylic acids, and ketones (Figure 2d). The CH_4 releases were related to the conversion of alkyl chains and the removal of methoxyl substituents in the SCR.[51] The generation of phenols and ethers at 300−600 °C was related to the dehydration reaction of the hydroxyl groups in the propane side chains followed by cleavage of ether linkages among the units in the SCR (Figure 2d).[46] In addition, the releases of alcohols at relatively high temperatures were likely associated with the ruptures of methoxy groups, methylene in the side chain, or the further cracking of volatiles.[46] The unconjugated C=O groups hardly produced at 300−400 °C (Figure 2d), which was likely because of the dissociation of unconjugated C=O groups to form the large releases of CO_2.[46,52] Therefore, the relative integral areas of the Gaussian peaks in TG-FTIR spectra were effective to accurately quantify the temperature-dependent changes in the gas amounts from biomass pyrolysis, avoiding the neglect and overquantification of hidden and prominent gaseous species.

Sequential Temperature Responses of the Gas Products. For a complicated system, such as SCR pyrolysis, gaseous species with different origins might have overlapping vibrational peaks that cannot be distinguished using simple TG-FTIR or TG-MS analysis. Fortunately, these overlapping peaks for different gaseous species had different responses to the pyrolysis temperature. Such delicate but important differences, correlations, and sequential changes in response to temperature could be better understood using 2D COS analysis. Therefore, for the SCR pyrolysis, the synchronous and asynchronous maps derived from 2D COS analysis helped facilitate the identification of the dynamic changes of gases under the perturbation of pyrolysis temperature (Figure 3a,b). The cross peaks at the bottom-right corner of the synchronous and asynchronous maps from the 2D-TG-FTIR-COS analysis were counted and analyzed (Figure 3a,b). The complicated peak distributions in the synchronous and asynchronous maps also indicated the complex thermal reactions that were occurring during SCR pyrolysis (Figure 3a,b). The assignments and signs of the peaks in the synchronous and asynchronous maps derived from 2D COS analysis are shown in Tables S5 and S7. In the synchronous map, three auto peaks were found near the wavenumbers ($\nu1/\nu2$) of 2336/2336 cm^{-1}, 1770/1770 cm^{-1}, and 1142/1142 cm^{-1} along the diagonal line, which were associated with gas products of CO_2, carboxylic acids/ketones, and ethers, respectively (Figure 3a). Five positive cross peaks at 2336/(1764, 1154, 670) cm^{-1} and 1770/(1170, 670) cm^{-1} were observed off the diagonal line in the synchronous map (Figure 3a). Therefore, based on Noda's rules,[53] the carboxylic acids and ketones simultaneously changed with CO_2 and ethers as the pyrolysis temperature increased. Additionally, the synchronous map also exhibited two weak off-diagonal peaks with negative signals at 3828/(2340, 542) cm^{-1} (Figure 3a), indicating that the spectral changes for H_2O and CO_2 proceeded in different directions with pyrolysis temperature.

An asynchronous map from the 2D-TG-FTIR-COS analysis of the SCR pyrolysis can reveal the sequential changes in different wavenumbers as a function of pyrolysis temperature. Five main negative cross peaks or regions with wavenumbers of 2336/1715 cm^{-1}, 2336/(1230−1548) cm^{-1}, 2336/1092 cm^{-1}, 1794/1736 cm^{-1}, and 1794/(1254−1552) cm^{-1} appeared off the diagonal line in the asynchronous map (Figure 3b). In addition, three weak negative cross peaks were also observed at 2336/(2146, 492) cm^{-1} and 1794/1080 cm^{-1} in the asynchronous map (Figure 3b). On the basis of Noda's rules,[53] the sequential changes in wavenumbers followed the orders of: (1736, 1254−1552, 1080) > 1794 cm^{-1}, and (2146, 1715, 1230−1548, 1092, 492) > 2336 cm^{-1}. Therefore, it can be concluded that the sequential temperature responses for the gas products generally occurred in the orders of phenols/alkanes/aromatics/alcohols > carboxylic acids/ketones > CO_2, and CO > CO_2. Additionally, the sequential changes in the wavenumbers with the orders of 1736 > 1794 cm^{-1} and 492 > 2336 cm^{-1} suggested that different responses to changes in temperature occurred even in the same gas products (i.e., carboxylic acids, ketones and CO_2). This result may have been due to the thermal decomposition of different components in the SCR that occurred at different pyrolysis temperatures. Moreover, six main positive peaks or regions at the wavenumbers of (3506−3948)/2346 cm^{-1}, (3530−3928)/1790 cm^{-1}, (1736, 1522)/1170 cm^{-1}, and (1736, 1522)/654 cm^{-1}, and four weak positive peaks at the wavenumbers of 3744/(1170, 654) cm^{-1} and 2942/(2346, 1792) cm^{-1} were observed in the asynchronous map (Figure 3b). Therefore, the sequential changes in the wavenumbers followed the order of (3744, 1736, 1522) > (654, 1170) cm^{-1}, (3530−3928) > 1790 cm^{-1}, (3506−3948) > 2346 cm^{-1}, and 2942 > (2346, 1792) cm^{-1}. This result suggested that the sequential temperature responses for gas products generally occurred in the orders of H_2O/CH_4 > carboxylic acids/ketones > CO_2/ethers, and aromatics > CO_2/ethers.

Along with the TG-FTIR and TG-MS probes, the hetero 2D-TG-FTIR/MS-COS provided complementary and comprehensive insights into the temperature responses and correlations for gaseous species from SCR pyrolysis. The heterosynchronous and heteroasynchronous maps with FTIR wavenumbers ($\nu1$) on the x-axis and MS m/z values ($\nu2$) on the y-axis are shown in Figure 3c,d. In general, as shown in the

DOI: 10.1021/acs.est.9b04595
Environ. Sci. Technol. 2019, 53, 13495−13505

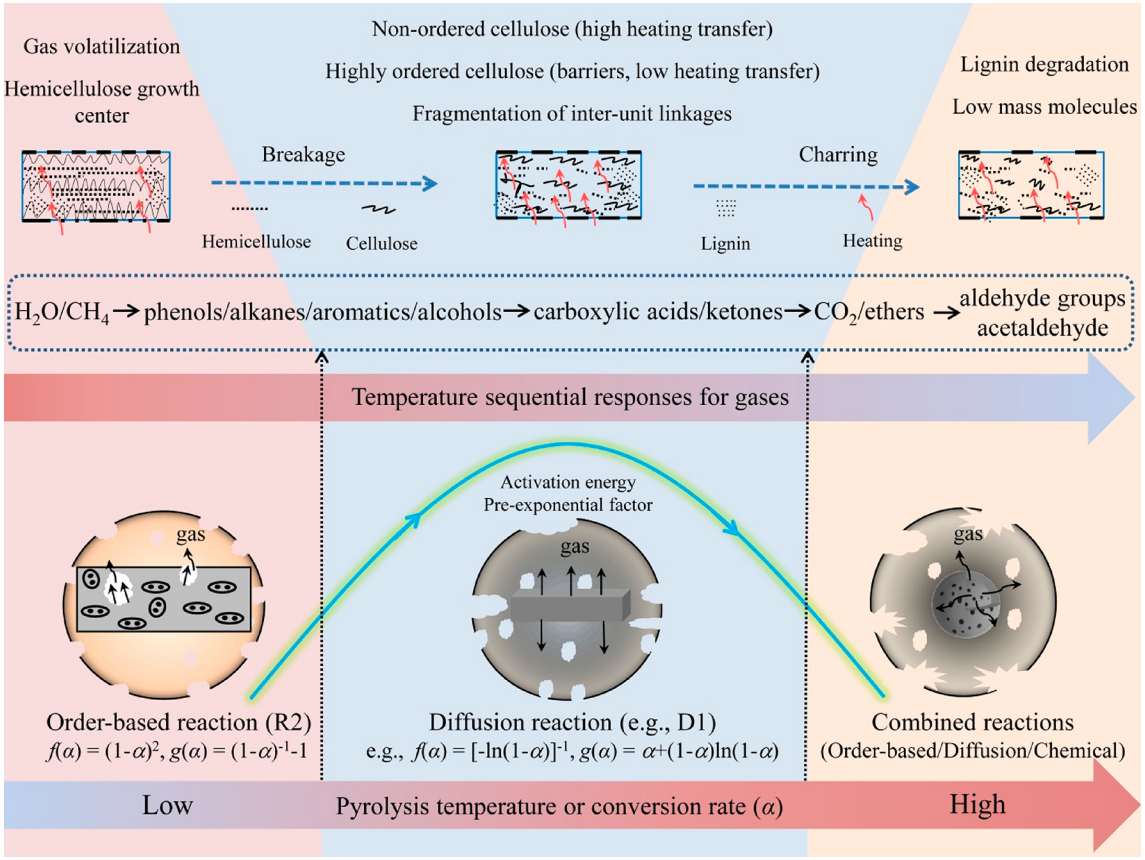

Figure 4. Schematic illustration of temperature response mechanism for SCR pyrolysis.

heterosynchronous map, the MS m/z values at 16 and 29 were positively correlated with main FTIR wavenumbers of approximately 662, 1092, 1170, 1742, 2178, 2320, 2946, and 3738 cm^{-1} (Figure 3c). This result indicated that the gas products of the CH_4 and aldehyde groups were positively correlated with most of the gas products (e.g., alcohols and ethers) released from the pyrolysis of SCR. Additionally, three main regions of the cross peaks at the m/z of 16 (negative signal), 18 (negative signal), and 29 (positive signal) with the corresponding main FTIR wavenumbers of approximately 600−1800 cm^{-1}, 2140, 2334, 2942, and 3584 cm^{-1} were observed in the heteroasynchronous map (Figure 3d). It can be concluded that the H_2O/CH_4 and aldehyde groups gave the fastest and slowest pyrolysis temperature responses among most of the gas products. Two weak regions of the cross peaks at the m/z of 31 (negative signal) and 43 (positive signal) with the corresponding main FTIR wavenumbers of 1150, 1764, and 2334 cm^{-1} also appeared in the heteroasynchronous map (Figure 3d). Therefore, the sequences of m/z and wavenumbers followed the order of 31 > (1150, 1764, 2334) cm^{-1} > 43, suggesting that the sequential temperature responses of gas products occurred in the order of alcohol groups > ethers/carboxylic acids/ketones/CO_2 > acetaldehyde. The 2D-TG-FTIR-COS and hetero 2D-TG-FTIR/MS-COS results when combined with the summary results found in this study demonstrated for the first time that the temperature responses of gas products from the pyrolysis of SCR followed the main order of H_2O/CH_4 > phenols/alkanes/aromatics/alcohols > carboxylic acids/ketones > CO_2/ethers > aldehyde groups/acetaldehyde. The sequential temperature responses of the gas products for SCR pyrolysis were related to the complicated physicochemical processes. The components in the SCR might first undergo dehydration, bond breakage, and fragmentation of the relatively macromolecular components (e.g., aromatics and carboxylic acids).[54] Then, the gaseous species with low molecular weight (e.g., acetaldehyde) might release due to depolymerization, secondary reactions, and interactions of components or gaseous species at higher SCR pyrolysis temperatures.[54]

Pyrolysis Temperature Response Mechanism. A novel temperature response mechanism for SCR pyrolysis is proposed in this study (Figure 4). The order-based reaction mechanisms for the solid-state reaction of SCR (i.e., R2) mainly appeared at lower conversion rates (α < 0.3) (Figure 4). This could actually be interpreted as a nucleation process in which the nuclei grow by collision with each other.[3] The primary mechanism R2 for the order-based reaction mechanism was related to the faster degradation of SCR. A greater population of growth centers was developed for the ruptures of ordered chains during the degradation reactions.[30] Combined with the order-based reaction mechanisms, the fast temperature responses of H_2O and CH_4 at lower conversion rates were primary associated with water evaporation and the release or degradation of volatiles from the SCR particle pores with heat transfer (Figure 4).[1] Hemicellulose is considered an amorphous component, whereas cellulose is a semicrystalline polymeric material containing both crystalline and amorphous components.[13] Therefore, at lower conversion rates, the temperature responses for some phenols, alkanes, aromatics, and alcohols were associated with the ruptures of some nonordered chains in hemicellulose, which might act as a center of random nucleation and growth during the SCR

DOI: 10.1021/acs.est.9b04595
Environ. Sci. Technol. 2019, 53, 13495−13505

degradation.[30] The diffusion reaction mechanisms of SCR (i.e., D1, Zh, and GB) primary occurred at relatively higher conversion rates (α = 0.4−0.7) (Figure 4). This result indicated that the reaction rate of SCR pyrolysis was primary controlled by diffusion as the conversion rate or pyrolysis temperature increased. For example, the Zh and GB mechanisms for solid-state reactions were a function of the diffusion of heat or hot gases from the SCR particles.[30] Most of the gas products were produced during the diffusion reaction processes, in which the temperature responses for the phenols, alkanes, aromatics, and alcohols were faster than those for the carboxylic acids and ketones (Figure 4). Nonordered cellulose in the SCR caused the rapid degradation of compounds with a lesser molecular mass. However, highly ordered cellulose regions might act as barriers to heat transfer and obstruct the degradation of cellulose, increasing the fiber thermal stability (Figure 4).[13,55] Therefore, the poor thermal conductivity caused nonuniform heating and thermal decomposition, as well as limiting diffusion.[34] Pyrolytic degradation of nonordered cellulose in the SCR might involve the fragmentation of interunit linkages. From this degradation process, the releasing macromolecular components (e.g., monomeric phenols or aromatics) into the vapor phase could accelerate the degradation process.[13,56] With an increasing pyrolysis temperature, the relatively small components, such as carboxylic acids and ketones, released during further degradation of nonordered or ordered cellulose in the SCR. At a high conversion rate (e.g., α = 0.8), order-based, diffusion, and chemical reaction mechanisms (e.g., F1) all appeared, which might be associated with the thermal degradation of lignin (Figure 4). The lignin degradation in SCR required more energy to destroy the relatively strong bonds.[40] At high conversion rates, the temperature responses of CO_2 and ethers were faster than those of the aldehyde groups and acetaldehyde (Figure 4). As the temperature and conversion rate increased, the interactions among the internal products also caused the production of fewer molecular mass molecules.[54] However, other preliminary data showed that a small heating rate range for SCR slow pyrolysis might have a limited influence on the temperature response mechanisms of the evolved gases. This phenomenon might be because the small heating rate range was difficult to significantly affect the reaction pathways, secondary reactions, and sequential responses of gaseous species to temperature. The component degradation or gas generation from the biomass pyrolysis is also related to the types and heterogeneous structures of the biomass. Therefore, the temperature sequencing releases of gas products from the pyrolysis of different biomasses may be different under various conditions, which need to be further investigated by novel 2D COS and hetero 2D COS analyses.

Implications. The first proposal of a novel temperature response mechanism at the molecular level was obtained from this study, establishing links between the solid-state reactions and gas-state dynamics of biomass pyrolysis. One of the novelties of this study revealed, for the first time, that the primary sequential responses of gaseous species to temperature during SCR pyrolysis occurred in the order of H_2O/CH_4 > phenols/alkanes/aromatics/alcohols > carboxylic acids/ketones > CO_2/ethers > aldehyde groups/acetaldehyde using novel 2D-TG-FTIR-MS-COS analysis. Subtle sequential changes to the temperature even occurred within the same gaseous species during the SCR pyrolysis. Gaussian deconvolution with TG-FTIR spectra was innovatively developed to distinguish the hidden or weak peaks and accurately quantify the amount of evolved gases, especially for low concentration gases. The temperature-dependent changes in gas amounts and sequential responses of gases were fitted to the combined effects of the order-based (primarily at α < 0.3), diffusion (primarily at α = 0.4−0.7), and chemical reaction mechanisms for the degradation of different components in the SCR. Additionally, the thermodynamic parameters defined using a new thermal model implied that the heating rates affected the decomposition contribution rates and mass loss rates of the pseudocomponents in the SCR.

The new findings of this study have several implications for future studies of biomass pyrolysis. (1) The feasibility of the Gaussian model, 2D COS, and hetero 2D COS platforms for TG-FTIR-MS analysis make it possible to provide a novel perspective on the kinetics, evolved gases, and mechanisms for biomass pyrolysis. The flexibility of the Gaussian model allows for the accurate identification and quantification of different pseudocomponents and gaseous species resulting from biomass pyrolysis. In addition, the 2D COS and hetero 2D COS with high detection sensitivities and capabilities were proven for the first time to be effective for probing the specific sequencing responses and hetero correlations of the gaseous species as a function of the pyrolysis temperature. (2) A direct link between the experimental dynamic data and the reaction mechanism can be achieved using the comprehensive knowledge obtained from the novel techniques and a defined thermal model in this study. The establishment of the novel temperature response mechanism at the molecular level contributes to our understanding of the complex challenging kinetics and solid−gas reactions of biomass pyrolysis. In addition, the resolution of thermodynamic parameters and reaction conditions found using the thermal models will be critical for optimizing the pyrolysis process performance. (3) The TG-FTIR-MS combined with the Gaussian model, 2D COS, and hetero 2D COS are promising approaches for online and real-time monitoring and quantification of the temperature-dependent dynamics of evolved gaseous species. These promising approaches are beneficial for designing favorable strategies for gas management, byproduct recovery, and energy utilization. However, the present study only tested a specific biomass; therefore, the results might not be sufficient. It is expected that this preliminary study will serve as a "first spark" to provide new techniques and advancements for investigations of pyrolysis processes of various biomasses in the future.

■ ASSOCIATED CONTENT

Supporting Information

The Supporting Information is available free of charge on the ACS Publications website at DOI: 10.1021/acs.est.9b04595.

Preparation and characterization of SCR, analysis models, results and discussion of the additional important points and supplementary figures and tables (PDF)

■ AUTHOR INFORMATION

Corresponding Author

*Tel: +86-10-84931804. Fax: +86-10-84931804. E-mail: baiyc@craes.org.cn.

ORCID

Yingchen Bai: 0000-0003-2869-422X

Baoshan Xing: 0000-0003-2028-1295

DOI: 10.1021/acs.est.9b04595
Environ. Sci. Technol. 2019, 53, 13495−13505

Fengchang Wu: 0000-0003-2615-2849

Notes

The authors declare no competing financial interest.

■ ACKNOWLEDGMENTS

This work was financially supported by the National Natural Science Foundation of China (Nos. 41521003, 41630645 and 41573130).

■ REFERENCES

(1) Liang, F.; Wang, R.; Xiang, H.; Yang, X.; Zhang, T.; Hu, W.; Mi, B.; Liu, Z. Investigating pyrolysis characteristics of moso bamboo through TG-FTIR and Py-GC/MS. *Bioresour. Technol.* **2018**, *256*, 53−60.

(2) Wang, X.; Chen, G.; Wang, S.; Zhang, L.; Zhang, R. Temperature sensitivity of different soil carbon pools under biochar addition. *Environ. Sci. Pollut. Res.* **2019**, *26* (4), 4130−4140.

(3) Wang, X.; Hu, M.; Hu, W.; Chen, Z.; Liu, S.; Hu, Z.; Xiao, B. Thermogravimetric kinetic study of agricultural residue biomass pyrolysis based on combined kinetics. *Bioresour. Technol.* **2016**, *219*, 510−520.

(4) Peters, J. F.; Iribarren, D.; Dufour, J. Biomass pyrolysis for biochar or energy applications? A life cycle assessment. *Environ. Sci. Technol.* **2015**, *49* (8), 5195−5202.

(5) Chen, L.; Xing, L.; Han, L. Renewable energy from agro-residues in China: Solid biofuels and biomass briquetting technology. *Renewable Sustainable Energy Rev.* **2009**, *13* (9), 2689−2695.

(6) Gabra, M.; Pettersson, E.; Backman, R.; Kjellström, B. Evaluation of cyclone gasifier performance for gasification of sugar cane residue—Part 1: gasification of bagasse. *Biomass Bioenergy* **2001**, *21* (5), 351−369.

(7) Jeong, C. Y.; Dodla, S. K.; Wang, J. J. Fundamental and molecular composition characteristics of biochars produced from sugarcane and rice crop residues and by-products. *Chemosphere* **2016**, *142*, 4−13.

(8) Deng, W.; Wu, W.; Wang, H.; Luo, W.; Kimberley, M. O. Temporal dynamics of iron-rich, tropical soil organic carbon pools after land-use change from forest to sugarcane. *J. Soils Sediments* **2009**, *9* (2), 112−120.

(9) Zhao, B.; O'Connor, D.; Zhang, J.; Peng, T.; Shen, Z.; Tsang, D. C. W.; Hou, D. Effect of pyrolysis temperature, heating rate, and residence time on rapeseed stem derived biochar. *J. Cleaner Prod.* **2018**, *174*, 977−987.

(10) Angın, D. Effect of pyrolysis temperature and heating rate on biochar obtained from pyrolysis of safflower seed press cake. *Bioresour. Technol.* **2013**, *128*, 593−597.

(11) Chen, D.; Zhou, J.; Zhang, Q. Effects of heating rate on slow pyrolysis behavior, kinetic parameters and products properties of moso bamboo. *Bioresour. Technol.* **2014**, *169*, 313−319.

(12) Dhyani, V.; Kumar, J.; Bhaskar, T. Thermal decomposition kinetics of sorghum straw via thermogravimetric analysis. *Bioresour. Technol.* **2017**, *245*, 1122−1129.

(13) Poletto, M.; Júnior, H. L. O.; Zattera, A. J. Thermal decomposition of natural fibers: Kinetics and degradation mechanisms. *Reactions and Mechanisms in Thermal Analysis of Advanced Materials* **2015**, 515−545.

(14) Ding, Y.; Huang, B.; Wu, C.; He, Q.; Lu, K. Kinetic model and parameters study of lignocellulosic biomass oxidative pyrolysis. *Energy* **2019**, *181*, 11−17.

(15) Fang, S.; Yu, Z.; Ma, X.; Lin, Y.; Chen, L.; Liao, Y. Analysis of catalytic pyrolysis of municipal solid waste and paper sludge using TG-FTIR, Py-GC/MS and DAEM (distributed activation energy model). *Energy* **2018**, *143*, 517−532.

(16) Ahamad, T.; Alshehri, S. M. TG−FTIR−MS (evolved gas analysis) of bidi tobacco powder during combustion and pyrolysis. *J. Hazard. Mater.* **2012**, *199−200*, 200−208.

(17) Ren, Q.; Zhao, C. NOx and N_2O precursors from biomass pyrolysis: Role of cellulose, hemicellulose and lignin. *Environ. Sci. Technol.* **2013**, *47* (15), 8955−8961.

(18) Tian, B.; Qiao, Y. Y.; Tian, Y. Y.; Xie, K. C.; Liu, Q.; Zhou, H. F. FTIR study on structural changes of different−rank coals caused by single/multiple extraction with cyclohexanone and NMP/CS_2 mixed solvent. *Fuel Process. Technol.* **2016**, *154*, 210−218.

(19) Liu, F. J.; Wei, X. Y.; Xie, R. L.; Wang, Y. G.; Li, W. T.; Li, Z. K.; Li, P.; Zong, Z. M. Characterization of oxygen-containing species in methanolysis products of the extraction residue from Xianfeng lignite with negative-ion electrospray ionization Fourier transform ion cyclotron resonance mass spectrometry. *Energy Fuels* **2014**, *28* (9), 5596−5605.

(20) Song, F.; Wu, F.; Xing, B.; Li, T.; Feng, W.; Giesy, J. P.; Guo, W.; Wang, H.; Liu, S.; Bai, Y. Protonation-dependent heterogeneity in fluorescent binding sites in sub-fractions of fulvic acid using principle component analysis and two-dimensional correlation spectroscopy. *Sci. Total Environ.* **2018**, *616−617*, 1279−1287.

(21) Noda, I.; Ozaki, Y. Two-Dimensional Correlation Spectroscopy - Applications in Vibrational and Optical Spectroscopy. *Chapter 4. Generalized two-dimensional correlation spectroscopy in practice* **2009**, 47−64.

(22) Hur, J.; Jung, K. Y.; Jung, Y. M. Characterization of spectral responses of humic substances upon UV irradiation using two-dimensional correlation spectroscopy. *Water Res.* **2011**, *45* (9), 2965−2974.

(23) Chen, W.; Teng, C. Y.; Qian, C.; Yu, H. Q. Characterizing properties and environmental behaviors of dissolved organic matter using two-dimensional correlation spectroscopic analysis. *Environ. Sci. Technol.* **2019**, *53* (9), 4683−4694.

(24) Chen, W.; Habibul, N.; Liu, X. Y.; Sheng, G. P.; Yu, H. Q. FTIR and synchronous fluorescence heterospectral two-dimensional correlation analyses on the binding characteristics of copper onto dissolved organic matter. *Environ. Sci. Technol.* **2015**, *49* (4), 2052−2058.

(25) Noda, I. Two-dimensional infrared (2D IR) spectroscopy: Theory and applications. *Appl. Spectrosc.* **1990**, *44* (44), 550−561.

(26) Phong, D. D.; Hur, J. Using two-dimensional correlation size exclusion chromatography (2D-CoSEC) and EEM-PARAFAC to explore the heterogeneous adsorption behavior of humic substances on nanoparticles with respect to molecular sizes. *Environ. Sci. Technol.* **2018**, *52* (2), 427−435.

(27) Sriram, A.; Swaminathan, G. Pyrolysis of Musa balbisiana flower petal using thermogravimetric studies. *Bioresour. Technol.* **2018**, *265*, 236−246.

(28) Xu, Y.; Chen, B. Investigation of thermodynamic parameters in the pyrolysis conversion of biomass and manure to biochars using thermogravimetric analysis. *Bioresour. Technol.* **2013**, *146*, 485−493.

(29) Criado, J. M. Kinetic analysis of DTG data from master curves. *Thermochim. Acta* **1978**, *24* (1), 186−189.

(30) Mallick, D.; Poddar, M. K.; Mahanta, P.; Moholkar, V. S. Discernment of synergism in pyrolysis of biomass blends using thermogravimetric analysis. *Bioresour. Technol.* **2018**, *261*, 294−305.

(31) Lin, Y.; Liao, Y.; Yu, Z.; Fang, S.; Ma, X. A study on co-pyrolysis of bagasse and sewage sludge using TG-FTIR and Py-GC/MS. *Energy Convers. Manage.* **2017**, *151*, 190−198.

(32) Lee, B. M.; Hur, J. Adsorption behavior of extracellular polymeric substances on graphene materials explored by fluorescence spectroscopy and two-dimensional Fourier transform infrared correlation spectroscopy. *Environ. Sci. Technol.* **2016**, *50* (14), 7364−7372.

(33) Chen, W.; Qian, C.; Liu, X. Y.; Yu, H. Q. Two-dimensional correlation spectroscopic analysis on the interaction between humic acids and TiO_2 nanoparticles. *Environ. Sci. Technol.* **2014**, *48* (19), 11119−11126.

(34) Ma, Z.; Chen, D.; Jie, G.; Bao, B.; Zhang, Q. Determination of pyrolysis characteristics and kinetics of palm kernel shell using TGA−FTIR and model-free integral methods. *Energy Convers. Manage.* **2015**, *89*, 251−259.

DOI: 10.1021/acs.est.9b04595
Environ. Sci. Technol. 2019, 53, 13495−13505

(35) Ahmad, M. S.; Mehmood, M. A.; Liu, C. G.; Tawab, A.; Bai, F. W.; Sakdaronnarong, C.; Xu, J.; Rahimuddin, S. A.; Gull, M. Bioenergy potential of Wolffia arrhiza appraised through pyrolysis, kinetics, thermodynamics parameters and TG-FTIR-MS study of the evolved gases. *Bioresour. Technol.* **2018**, *253*, 297−303.
(36) Yustiawati; Kihara, Y.; Sazawa, K.; Kuramitz, H.; Kurasaki, M.; Saito, T.; Hosokawa, T.; Syawal, M. S.; Wulandari, L.; Hendri, I.; Tanaka, S. Effects of peat fires on the characteristics of humic acid extracted from peat soil in Central Kalimantan, Indonesia. *Environ. Sci. Pollut. Res.* **2015**, *22* (4), 2384−2395.
(37) Maia, A. A. D.; De Morais, L. C. Kinetic parameters of red pepper waste as biomass to solid biofuel. *Bioresour. Technol.* **2016**, *204*, 157−163.
(38) Yin, S.; Rajarao, R.; Sahajwalla, V. Thermal transformation of metallized plastic packaging waste into value-added Al/Al_3C_4/AlN resources. *ACS Sustainable Chem. Eng.* **2019**, *7* (1), 1723−1733.
(39) Broido, A.; Nelson, M. A. Char yield on pyrolysis of cellulose. *Combust. Flame* **1975**, *24*, 263−268.
(40) Yang, H.; Yan, R.; Chin, T.; Liang, D. T.; Chen, H.; Zheng, C. Thermogravimetric analysis-Fourier transform infrared analysis of palm oil waste pyrolysis. *Energy Fuels* **2004**, *18* (6), 1814−1821.
(41) Vlaev, L. T.; Georgieva, V. G.; Genieva, S. D. Products and kinetics of non-isothermal decomposition of vanadium(IV) oxide compounds. *J. Therm. Anal. Calorim.* **2007**, *88* (3), 805−812.
(42) Rony, A. H.; Kong, L.; Lu, W.; Dejam, M.; Adidharma, H.; Gasem, K. A. M.; Zheng, Y.; Norton, U.; Fan, M. Kinetics, thermodynamics, and physical characterization of corn stover (Zea mays) for solar biomass pyrolysis potential analysis. *Bioresour. Technol.* **2019**, *284*, 466−473.
(43) Vlaev, L. T.; Markovska, I. G.; Lyubchev, L. A. Non-isothermal kinetics of pyrolysis of rice husk. *Thermochim. Acta* **2003**, *406*, 1−7.
(44) Singh, S.; Wu, C.; Williams, P. T. Pyrolysis of waste materials using TGA-MS and TGA-FTIR as complementary characterisation techniques. *J. Anal. Appl. Pyrolysis* **2012**, *94*, 99−107.
(45) Liu, Q.; Wang, S.; Zheng, Y.; Luo, Z.; Cen, K. Mechanism study of wood lignin pyrolysis by using TG−FTIR analysis. *J. Anal. Appl. Pyrolysis* **2008**, *82* (1), 170−177.
(46) Wang, S.; Lin, H.; Ru, B.; Sun, W.; Wang, Y.; Luo, Z. Comparison of the pyrolysis behavior of pyrolytic lignin and milled wood lignin by using TG−FTIR analysis. *J. Anal. Appl. Pyrolysis* **2014**, *108*, 78−85.
(47) Kai, X.; Li, R.; Yang, T.; Shen, S.; Ji, Q.; Zhang, T. Study on the co-pyrolysis of rice straw and high density polyethylene blends using TG-FTIR-MS. *Energy Convers. Manage.* **2017**, *146*, 20−33.
(48) Kai, X.; Yang, T.; Shen, S.; Li, R. TG-FTIR-MS study of synergistic effects during co-pyrolysis of corn stalk and high-density polyethylene (HDPE). *Energy Convers. Manage.* **2019**, *181*, 202−213.
(49) Yuan, H.; Fan, H.; Shan, R.; He, M.; Gu, J.; Chen, Y. Study of synergistic effects during co-pyrolysis of cellulose and high-density polyethylene at various ratios. *Energy Convers. Manage.* **2018**, *157*, 517−526.
(50) Părpăriţă, E.; Nistor, M. T.; Popescu, M. C.; Vasile, C. TG/FT−IR/MS study on thermal decomposition of polypropylene/biomass composites. *Polym. Degrad. Stab.* **2014**, *109*, 13−20.
(51) Özsin, G.; Pütün, A. E. Kinetics and evolved gas analysis for pyrolysis of food processing wastes using TGA/MS/FT-IR. *Waste Manage.* **2017**, *64*, 315−326.
(52) Jiang, Y.; Zong, P.; Tian, B.; Xu, F.; Tian, Y.; Qiao, Y.; Zhang, J. Pyrolysis behaviors and product distribution of Shenmu coal at high heating rate: A study using TG-FTIR and Py-GC/MS. *Energy Convers. Manage.* **2019**, *179*, 72−80.
(53) Noda I, O. Y. *Two-dimensional correlation spectroscopy: Applications in vibrational and optical spectroscopy*; John Wiley Sons: 2005.
(54) Lian, F.; Xing, B. Black carbon (biochar) in water/soil environments: Molecular structure, sorption, stability, and potential risk. *Environ. Sci. Technol.* **2017**, *51* (23), 13517−13532.
(55) Poletto, M.; Zattera, A. J.; Santana, R. M. C. Thermal decomposition of wood: Kinetics and degradation mechanisms. *Bioresour. Technol.* **2012**, *126*, 7−12.
(56) Tejado, A.; Peña, C.; Labidi, J.; Echeverria, J. M.; Mondragon, I. Physico-chemical characterization of lignins from different sources for use in phenol−formaldehyde resin synthesis. *Bioresour. Technol.* **2007**, *98* (8), 1655−1663.

DOI: 10.1021/acs.est.9b04595
Environ. Sci. Technol. 2019, 53, 13495−13505

Supporting Information

Novel Insights into the Kinetics, Evolved Gases, and Mechanisms for Biomass (Sugar Cane Residue) Pyrolysis

Fanhao Song,[‡,†] Tingting Li,[‡], Jin Zhang,[‡] Xiaojie Wang,[§] Yingchen Bai,[*,‡] John P. Giesy,[‡,⊥] Baoshan Xing,[∥] and Fengchang Wu,[‡]

[‡]State Key Laboratory of Environmental Criteria and Risk Assessment, Chinese Research Academy of Environmental Sciences, Beijing, 10012, China

[†]College of Water Sciences, Beijing Normal University, Beijing 100875, China

[§]Guangzhou Institute of Geochemistry, Chinese Academy of Sciences, Guangzhou 510640, China

[⊥]Department of Biomedical and Veterinary Biosciences and Toxicology Centre, University of Saskatchewan, Saskatoon, Saskatchewan, SK S7N 5B3, Canada

[∥]Stockbridge School of Agriculture, University of Massachusetts, Amherst, Massachusetts, 01003, United States

This *Supporting Information* file has 33 pages including 8 figures and 7 tables.

[*]Corresponding author: Tel.: +86-10-84931804; Fax: +86-10-84931804.

E-mail: baiyc@craes.org.cn (Yingchen Bai)

Supporting Contents

Figure Captions

Figure S5. The plots of Ea (a), ΔH (b), and ΔG (c) values as a function of the conversion rate (α) of the SCR pyrolysis

Figure S6. Optimized decomposition process of hemicellulose, cellulose, and lignin pseudo-components in the SCR at four heating rates

Figure S7. The 3D FTIR spectrum (a), FTIR spectra at selected pyrolysis temperatures (b) and temperature-dependent curves of the primary MS ionized fragments (c) for the primary analysis of gas products from the SCR pyrolysis

Figure S8. Curve fitting of the TG-FTIR spectra at the selected temperatures of 200, 400, and 600 ℃ for the analysis of gases

Table Captions

Table S1. Structural parameters derived from the quantitative ^{13}C NMR spectroscopy

Table S2. Theoretical models of pyrolysis reactions with different $f(\alpha)$ and $g(\alpha)$ functions

Table S3. Thermodynamic parameters of the SCR pyrolysis derived from the FWO and DAEM methods at different conversion rates

Table S4. Optimized decomposition parameters of SCR pyrolysis at different heating rates

Table S5. Typical absorption peaks and their corresponding volatile gaseous species determined using TG-FTIR analysis

Table S6. Primary MS ion fragments and their corresponding possible volatile gaseous species

Table S7. The 2D-TG-FTIR-COS results on the assignments and signs of peaks in synchronous and asynchronous (in the brackets) maps for gas products from SCR pyrolysis.

References for Supporting Information

S1 Materials and Methods

S1.1 Preparation and Characterization of the SCR

The sugar cane residue (SCR) was obtained from the Sugarcane Research Institute, Guangdong Province, China. The SCR was dried at 100 ℃ for 3 h to reach a constant mass, ground into fine particles and passed through a 200-mesh sieve to achieve particle sizes less than 75 μm. The surface structures of the SCR were analyzed using scanning electron microscopy (SEM, JSM-6330F, Hitachi, Tokyo, Japan). The elemental composition, Fourier transform infrared (FTIR) spectra, and solid-state ^{13}C nuclear magnetic resonance (NMR) spectra of the SCR were determined according to the procedures in our previous study.[1] The thermogravimetric (TG) analysis and differential thermal analysis (DTA) for SCR pyrolysis were performed using thermo plus TG 8120, Rigaku, Japan. Additionally, the TG-FTIR-MS analysis for SCR pyrolysis was carried out using thermo-gravimetry coupled with FTIR spectrometry (TG-209/Vector-22, Netzsch/Bruke, Germany) and mass spectrometry (MS) (ThermoStar, Pfeiffer Vacuum). In detail, 20 mg of SCR was placed into a pipe furnace under an atmosphere of ultrapure nitrogen. The pyrolysis temperature of the SCR was set to increase from room temperature to 800 ℃ at each heating rate of 10, 20, 30, and 40 °C·min^{-1}. To reduce the effects of total thermos during the SCR pyrolysis, the TG experiment was conducted using temperature programming with each heating rate up to 800 ℃. Once the pyrolysis temperature reached 800 ℃, the temperature programming stopped immediately without maintained heating time. The actual pyrolysis time at each heating rate was significantly different and very close to the time obtained from the theoretical calculation. The volatile gases from the SCR pyrolysis at a heating rate of 20 °C·min^{-1} was detected using the FTIR spectrometer at a wavenumber range from 4000 cm^{-1} to 400 cm^{-1} with a resolution of 4 cm^{-1}. The volatile gases that passed through the FTIR spectrometer were analyzed

immediately using a mass spectrometer with a source of 70 eV electron energy. To avoid liquefaction of the volatile gases, the capillary lines were heated to temperatures of 250 ℃ and 270 ℃ for the FTIR spectrophotometer and mass spectrometer, respectively. The selected heating rate for analysis of the evolved gases of 20 °C·min^{-1} was beneficial for producing relatively higher gas amounts compared to 10 °C·min^{-1} and reducing the heat transfer limitation compared to 30 and 40 °C·min^{-1}.[2, 3] Additionally, a heating rate of 20 °C·min^{-1} for the SCR pyrolysis could provide the appropriate residence and detection time for the determination of intermediate gaseous species using the TG-FTIR-MS.

S1.2 Integral Methods

The conversion rate (α) at an absolute temperature of T (K) for the SCR pyrolysis can be expressed as Equation S1:

$$\alpha=\frac{m_{T_0}-m_T}{m_{T_0}-m_{T_f}} \quad \text{(S1)}$$

where m_{T_0}, m_T, and m_{T_f} are the initial mass at an initial temperature T_0, the actual mass at any temperature T, and the final mass at a final temperature T_f, respectively. Furthermore, the $\alpha(T)$ can be given as Equation S2:

$$\alpha(T)=\int_0^{\infty}\left\{1-\exp\left[-\frac{A}{\beta}\int_0^{T}\exp(-\frac{Ea}{RT}dT)\right]\right\}G(Ea)dE \quad \text{(S2)}$$

where β and R represent the constant heating rate and universal gas constant (R = 8.3145 J mol^{-1}·K^{-1}), respectively. According to the mean activation energy (Em) and the standard variance (σ), the Gaussian distribution function ($G(Ea)$) can be expressed as Equation S3:

$$G(Ea)=\frac{1}{\sqrt{2\pi\sigma}}\exp\left[-\frac{(Ea-Em)^2}{2\alpha^2}\right] \quad \text{(S3)}$$

By combining of Equations S2 and S3, the $\frac{d\alpha(T)}{dT}$ can be given as Equation S4:

$$\frac{d\alpha(T)}{dT} = \int_0^{\infty} \frac{A}{\beta} \exp\left[-\frac{Ea}{RT} - \frac{A}{\beta}\int_0^{T} \exp\left(-\frac{Ea}{RT}\right) dT\right] G(x)dE \quad \text{(S4)}$$

Furthermore, with some mathematical simplification and approximation, the FWO and DAEM methods can be expressed as Equations S5 and S6, respectively:[4-6]

$$\ln(\beta) = \ln\left(\frac{A \cdot Ea}{R \cdot G(\alpha)}\right) - \frac{Ea}{RT} \quad \text{(S5)}$$

$$\ln\left(\frac{\beta}{T^2}\right) = \ln\frac{AR}{Ea} + 0.6075 - \frac{Ea}{RT} \quad \text{(S6)}$$

In this study, at an α range of 0.2–0.8 with an interval of 0.05, both the activation energy (Ea) and the pre-exponential factor (A) values were determined using the FWO and DAEM methods from the linear plots of $\log(\beta)$ and $\ln\left(\frac{\beta}{T^2}\right)$ versus $1/T$, respectively.

S1.3 Thermodynamic Parameters

The thermodynamic parameters, including the change in enthalpy (ΔH), Gibb's free energy (ΔG) and entropy (ΔS), were calculated using Equations S7–S9 to investigate the thermodynamic behaviors of the SCR.[7, 8]

$$\Delta H = Ea - RT \quad \text{(S7)}$$

$$\Delta G = Ea + RT_m ln\left(\frac{K_B T_m}{hA}\right) \quad \text{(S8)}$$

$$\Delta S = \Delta H - \frac{\Delta G}{T_m} \quad \text{(S9)}$$

where K_B, h and T_m represent the Boltzmann constant (1.381×10^{-23} J·K^{-1}), Plank's constant (6.626×10^{-34} J·s) and the DTG original peak temperature, respectively.

S1.4 PeakFit Analysis

The characteristic peaks in the derivative TG (DTG) curves and the TG-FTIR spectra of the SCR were distinguished and separated using the Gaussian model with the Software PeakFit 4.0 using the second derivative fitting algorithm. For the peak fitting process, the Shirley

background correction, loess algorithm, and second derive zero algorithm were conducted to remove background noise, smooth and subtract the baseline of the DTG curves and the TG-FTIR spectra.[9] In addition, the second derivative method was also used to fit the peaks in the DTG curves and the TG-FTIR spectra of the SCR. The type of fitted peak in the software was set as Spectroscopy and Gauss Amp. The height, width, and shape of the fitted peaks were modified using the high value of the correlation coefficient between the original and fitted curves.

S1.5 2D Correlation Spectroscopy for the TG-FTIR-MS Spectra

The auto and cross peaks can be observed at the main diagonal and off-diagonal positions in the synchronous map, respectively.[16,18,26] Only cross peaks appear at the off-diagonal positions in the asynchronous map.[16,18,26] Influenced by the external forcing functions, the auto peaks in the synchronous map are associated with the sensitivity of the correlation spectrum to changes in the spectral intensity.[10, 11] The cross peaks in the synchronous and asynchronous maps represent the changes in the spectral intensity of the spectral variables (i.e., $v1$ and $v2$) and the sequential order of spectral variations induced by a perturbation, respectively.[10-12] In the synchronous and asynchronous maps, the sign of auto peaks is always positive, while the sign of cross peaks can be either positive or negative.[11, 13] Based on Noda's rules, the spectral change at wavenumber $v1$ will precede the change at wavenumber $v2$ if the cross peaks in the synchronous and asynchronous maps have the same sign in a given wavenumber range; otherwise, the reaction process will be reversed.[11, 13, 14]

S2 Results and Discussion

S2.1 Physicochemical Properties of the SCR

The SEM features showed that the surface structures of the SCR were relatively complete with little meso-pores, macro-pores, or irregularly distributed fragments (Figure S1a). The mass

percentage of elemental carbon (C), hydrogen (H), oxygen (O), and nitrogen in the SCR was reported to be 46.10%, 6.01%, 44.6% and 0.50%, respectively.[1] For the analysis of the FTIR spectra, the stretching OH groups (~3600–3250 cm^{-1}) were abundant in the SCR, followed by -C=O stretching of -COOH groups (~1750–1590 cm^{-1}) and C-O-C groups (~1050 cm^{-1}) (Figure S1b).[1, 15, 16] Stronger peaks at approximately 75 and 105 ppm were observed in the ^{13}C NMR spectra (Figure S1b), which also indicated the greater contents of the CH-OH and C-O-C groups in the SCR.[1, 17, 18] The percentages of alkyl carbon (68.46%) and aryl carbon (28.33%) were much greater than those of carbonyl carbon (3.22%) and O-aryl (3.65%) (Table S1). Non-protonated aromatic carbon commonly existed in the fused aromatic rings, and its percentage (10.10%) was slightly lower than that (14.58%) of protonated aromatic carbon (Table S1). The values of aliphatic carbon, total polar carbon, $r_{npary/pary}$ (the ratio of non-protonated to protonated aromatic carbon) and aromaticity were 83.04%, 73.94%, 0.69 and 29.27, respectively (Table S1). This result indicated the SCR had the lower aromaticity and higher polarity compared to the biomass-derived biochars.[19, 20]

S2.2 Thermodynamic and Kinetic Characteristics of the SCR

Each heating rate for SCR pyrolysis kept nearly constant during the heating process, which basically established the non-isothermal conditions (Figure S3a).[21] It also suggested that the endothermic and exothermic reactions of the SCR pyrolysis had very slight effects on furnace temperature.[21] As shown in the TG and DTG curves at four heating rates, the weight losses of the SCR remained nearly constant prior to the pyrolysis temperature of 200 ℃ (Figure S3b), and this was primarily associated with the water evaporation and the release of volatiles from particle pores.[22] The weight losses at the first (200–325 ℃), second (325–390 ℃) and third (390–800 ℃) stages in the TG and DTG curves were primarily associated with the degradation of

hemicellulose, cellulose and lignin/fixed carbon in the SCR, respectively (Figure S3b).[21, 23] At the high temperature range of 700–800 ℃ for SCR pyrolysis, the mass loss at each heating rate kept nearly constant, indicating the polymer components in the SCR were almost completely transformed into gas products at each heating rate (Figure S3b). Furtherly, the preliminary qualitative data from the TG-FTIR analysis showed that the gas amounts released at 10 ℃·min^{-1} was slightly lower than those released at 20 ℃·min^{-1} during SCR pyrolysis. The high heat fluxes in the high heating regime slightly intensified the reactions forming volatiles during the SCR pyrolysis process.[24] In general, the small range of heating rates for the SCR slow pyrolysis had slight effects on the amounts of released gases. The thermal degradation of SCR at a heating rate of 10 ℃·min^{-1} was also determined using the DTA (Figures S3c, d). Four Gaussian peaks in the DTA curve were deconvoluted to investigate the endothermic and exothermic reactions during the SCR pyrolysis process (Figure S3c). The Gaussian peaks at 50 ℃ (Peak A) and 143 ℃ (Peak B) in the DTA curve were associated to endothermic reactions for the moisture release during SCR pyrolysis (Figure S3c).[25] In addition, the Gaussian peaks at 245 ℃ (Peak C) and 376 ℃ (Peak D) in the DTA curve were related to exothermic reactions for the dehydration, decarboxylation, and decomposition of components in the SCR (Figure S3c).[25] In detail, the exothermic reaction of Peak C was attributed to the decarboxylation reaction of the acidic groups, proteins, carbohydrates, and fatty acids in the SCR.[25, 26] The exothermic reaction of Peak D was related to the breakage of the aromatic structures and the cleavage of the C-C bonds in the SCR.[25, 26] The positions of the exothermic peaks of the SCR were shifted toward the lower temperatures compared to the exothermic peaks in the DTA curves of the organic matter.[25, 26] This result indicated that the SCR contained less resistant high-aromatic compounds compared to the reported organic matter.[23, 24] The areas of Gaussian peaks in the DTA curve of the SCR were

utilized to further estimate the endothermic and exothermic reactions (Figure S3d). The Gaussian peak areas for endothermic and exothermic reactions ranged from 187.57 to 276.21 $\mu V \cdot mg^{-1}$ (67.95%) and 94.74 to 124.01 $\mu V \cdot mg^{-1}$ (32.05%), respectively (Figure S3d). This result suggested that the endothermic energy for moisture release might be higher than the exothermic energy for the thermal degradation of compounds in the SCR prior to 600 ℃, such as the polysaccharides and hydroxyl aliphatic groups.

S2.3 Determination of the Thermodynamic Parameters

For the α-dependent changes in the *Ea* values of the SCR pyrolysis, slight increases in the *Ea* values at α = 0.20–0.25 were associated with the breakage of weakly linked bonds and the random scission on the polymeric lineal chain in hemicellulose (Figure S5a). The apparent increases in the *Ea* values at α = 0.30–0.45 were primarily attributed to the degradation of the cross-linked polymer matrix and the production of active cellulose (Figure S5a).[23] As an intermediate product during SCR pyrolysis, the active cellulose produced from the degradation of cellulose, resulted in a reduction of the molecular chain length and polymerization degree.[23, 27] In addition, significant decreases in the *Ea* values at α = 0.45–0.65 were related to the thermal degradation of active cellulose with a low molecular weight that required lower energy (Figure S5a).[23] The fluctuations in the *Ea* values at α = 0.65–0.75 might have been affected by the competitive degradation reactions among various cross-linked polymer matrices, and the block of internal minerals in the SCR (Figure S5a).[8] The rapid increases and relatively higher values of the *Ea* at α = 0.8 might be attributed to the interaction of internal components and the degradation of lignin, whose portion of the three-dimensional network structures required more energy during the SCR pyrolysis process (Figure S5a).[28]

Enthalpy denotes the total energy content required by pyrolysis to achieve the reaction temperature, representing the exchanged heat between the reactants and the activated compounds (e.g., lignocellulosic composition) in a thermal system.[7, 29] The enthalpy change (ΔH) represents the difference in the total formation energy between the reactants and the products (e.g., solid, liquid, and gaseous compositions).[29] The ΔH values of the SCR pyrolysis calculated using the FWO and DAEM methods were 204.88–266.88 kJ·mol^{-1} and 194.16–256.97 kJ·mol^{-1}, respectively (Table S3). The ΔH values of the SCR pyrolysis were higher than those of the pyrolysis of saw dust and rice husk blends (147.50–176.71 kJ·mol^{-1}), camel grass (79.44–188.01 kJ·mol^{-1}), rice straw (162.23–173.30 kJ·mol^{-1}), dairy manure (153.10–164.66 kJ·mol^{-1}), and chicken manure (158.91–175.30 kJ·mol^{-1}).[8, 29, 30] The obstruction of highly ordered components to heat diffusion might have caused the different energy of the dissociation of reactant bonds in the SCR and the biomasses discussed above. In addition, the ΔH values of the SCR pyrolysis showed the same α-dependent trends as the *Ea* values (Figures S5a, b). Mallick et al. (2018) also reported that the ΔH values of the pyrolysis of biomass blends were close to the corresponding *Ea* values with the differences being approximately 5 kJ·mol^{-1}.[29] The change in the Gibbs free energy (ΔG) represents an increase in the system energy for the activated complex formation.[8, 29] The ΔG values of the SCR pyrolysis (153.90–220.64 kJ·mol^{-1}) determined using both the FWO and DAEM methods were similar to those of the pyrolysis of rice straw (164.59 kJ·mol^{-1}), para grass (168–173 kJ·mol^{-1}), and rice husk and saw dust blends (175.70–181.82 kJ·mol^{-1}) in the published literatures (Table S3).[8, 29, 31] The ΔG values of the SCR pyrolysis all increased with increasing α values (Figure S5c), which was consistent with the results reported by Sriram and Swaminathan (2018) who found that the ΔG values of *Musa balbisiana* were higher at higher α values.[7] The change in entropy (ΔS) in the reaction system can represent the disorder degree,

247 which is associated with the arrangement degree of the carbon layers.[29] The negative and
248 positive values of ΔS indicate the attainment of thermal equilibrium and far from thermal
249 equilibrium in the reaction system, respectively.[29] The SCR pyrolysis system might have been
250 far from thermal equilibrium because of the near positive ΔS values of the SCR pyrolysis (Table
251 S3). In addition, the appearance of negative ΔS values determined using the FWO method at an α
252 range of 0.65–0.75 might be associated with the manifestation of complex and disordered
253 reactions during the conversion of the SCR into various products (Table S3).[29]

254 **S2.4 Releasing Characteristics of Gases Determined Using the TG-FTIR-MS**

255 The macromolecular polymers in the SCR can be pyrolyzed to produce small molecule gases
256 due to their cross-link polymerization and dehydrogenation oxidation.[32, 33] The 3D FTIR
257 spectrum, selected FTIR spectra, and MS evolution curves of the main ionized fragments are
258 shown in Figure S7 in the primary analysis of gases from SCR pyrolysis. The 3D FTIR spectrum
259 intuitively showed that the gas products varied greatly with pyrolysis temperature increasing, and
260 most of the gases were released from the SCR pyrolysis between 300 ℃ and 400 ℃ (Figure
261 S7a). The intensities of most absorption peaks in the TG-FTIR spectra decreased gradually or
262 disappeared in a pyrolysis temperature range of 500–600 ℃ (Figure S7b). The TG-FTIR
263 absorption peaks, primary TG-MS ionized fragments, and their corresponding possible volatile
264 gaseous species are shown and summarized in Figure S7 and Tables S5-S6.[22, 32, 34-37] As shown
265 in Figure S7b, the distinguished absorbance peaks at 3946, 3734 and 3588 cm^{-1} correspond to the
266 release of absorbed H_2O (O-H stretching), which was attributed to dehydration reactions (Table
267 S5). The absorbance peaks at 2926 and 2820 cm^{-1} indicated the formation of hydrocarbons,
268 especially for CH_4 (C-H stretching) (Figure S7b, Table S5). The absorbance peaks at 2358 and
269 668 cm^{-1} appeared when CO_2 (C=O stretching) was released from SCR pyrolysis (Figure S7b,

Table S5). Additionally, the absorbance peaks at 1796, 1510, and 1396 cm^{-1} were attributed to the releases of carboxylic acids/ketones (C-O stretching), aromatics (C-C stretching, benzene skeletal), and alkanes (C-H blending), respectively (Figure S7b, Table S5). The absorbance peaks at 1178 and 1122 cm^{-1} were related to the releases of ethers (C-O stretching) (Figure S7b, Table S5). In the present study, the Gaussian model had the advantages of finding overlapping and "hidden" peaks in the TG-FTIR spectra for the further analysis of gas products released from the SCR pyrolysis. Several weak or hidden peaks for CO (C-O stretching), unconjugated C=O groups (C=O stretching), phenols/ethers (C-O and O-H stretching), and alcohols (C-O and O-H stretching) were observed at 2159–2100 cm^{-1}, 1675–1647 cm^{-1}, 1297–1122 cm^{-1}, and 1100–992 cm^{-1}, respectively (Figures 2 and S8, Table S5).[23, 37] Moreover, similar gas products were also distinguished using MS analysis, such as the main ion fragments for CH_4, H_2O, C_2H_2 (acetylene), aldehydes, alcohols, C_3H_6 (propane), acetaldehyde, CO_2, formic acid, acetic acid/propanol/glycolaldehyde/methyl formate, and benzenes (Figure S7c, Table S6). Among the gaseous species from the MS analysis, acetaldehyde, formic acid and acetic acid were verified by the peaks of C=O stretching detected using the TG-FTIR analysis.[38] Moreover, the alcohol groups, propanol, glycolaldehyde, and methyl formate were associated with the peaks of C-O-H (1200 cm^{-1}) in the TG-FTIR spectra.

Figures

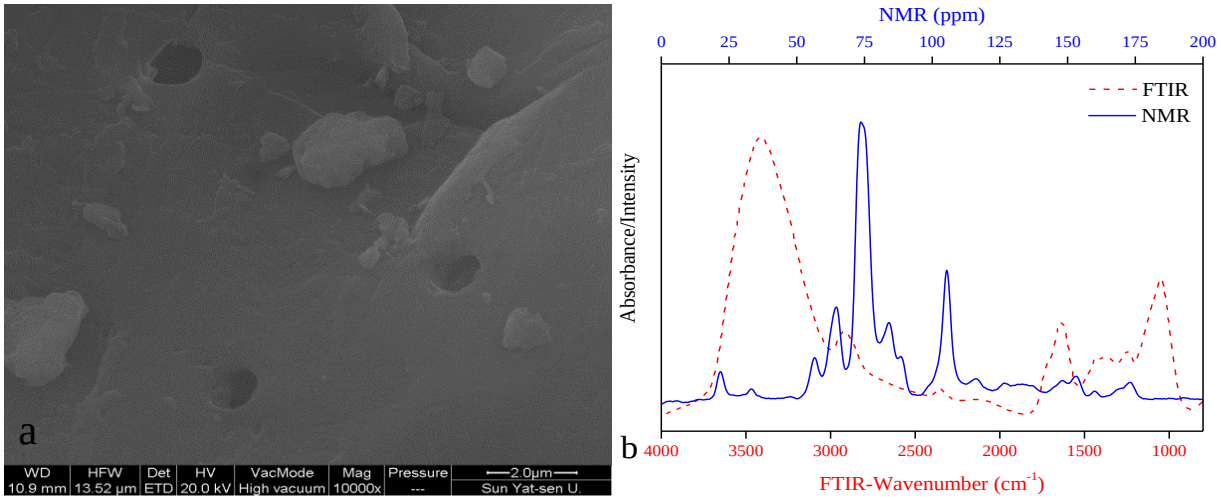

Figure S1. The SEM (a), FTIR, and ^{13}C NMR spectra (b)[1] of the SCR.

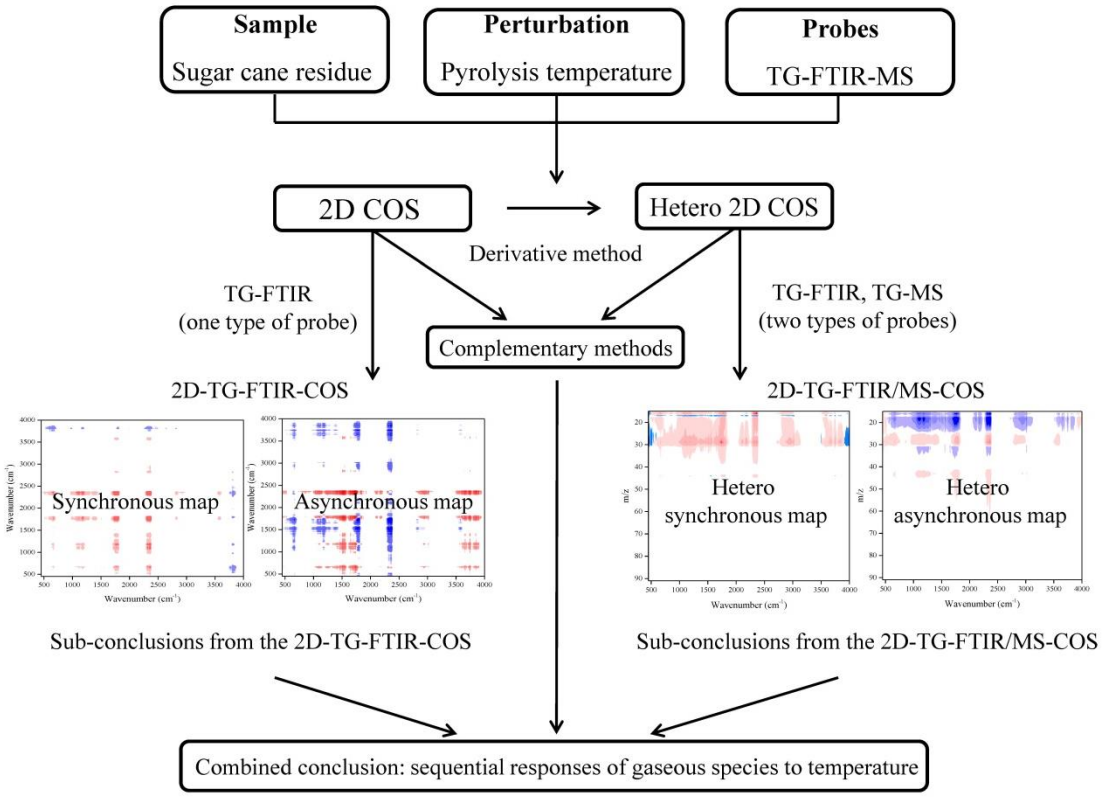

290

291 **Figure S2.** Schematic diagram for the TG-FTIR-MS combined with the 2D COS and hetero 2D

292 COS analyses.

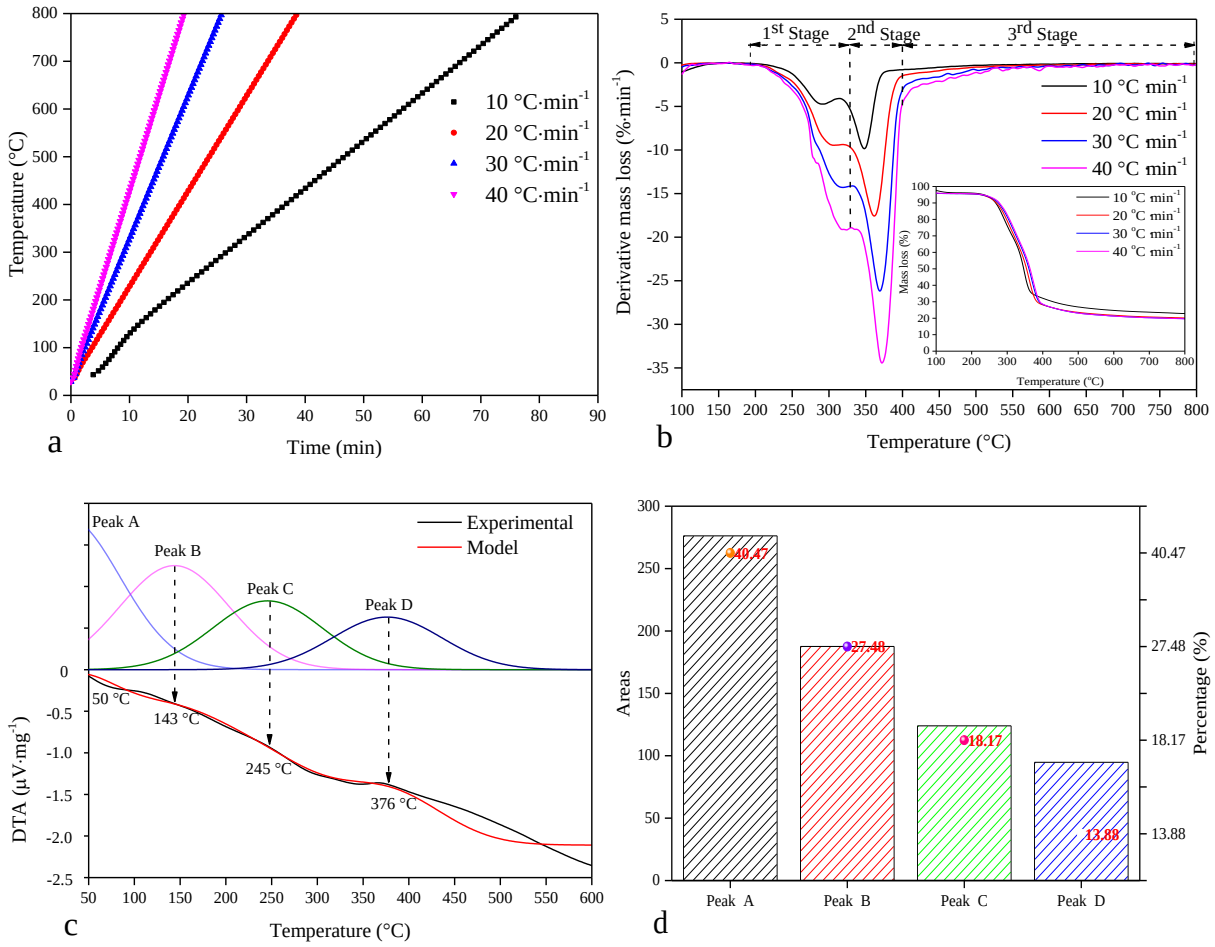

Figure S3. The temperature profiles (a), TG[1], and DTG curves (b) at four heating rates; deconvolution of the DTA curve (c) and the DTA Gaussian peak areas (d) at a heating rate of 10 ℃·min^{-1} of the SCR pyrolysis.

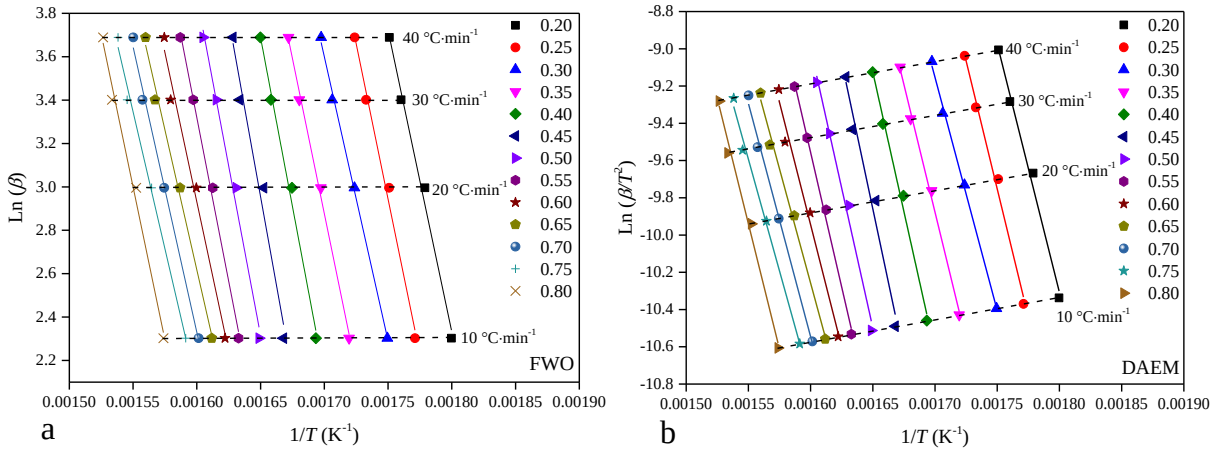

Figure S4. Arrhenius plots for FWO (a) and DAEM (b) at four heating rates of the SCR pyrolysis.

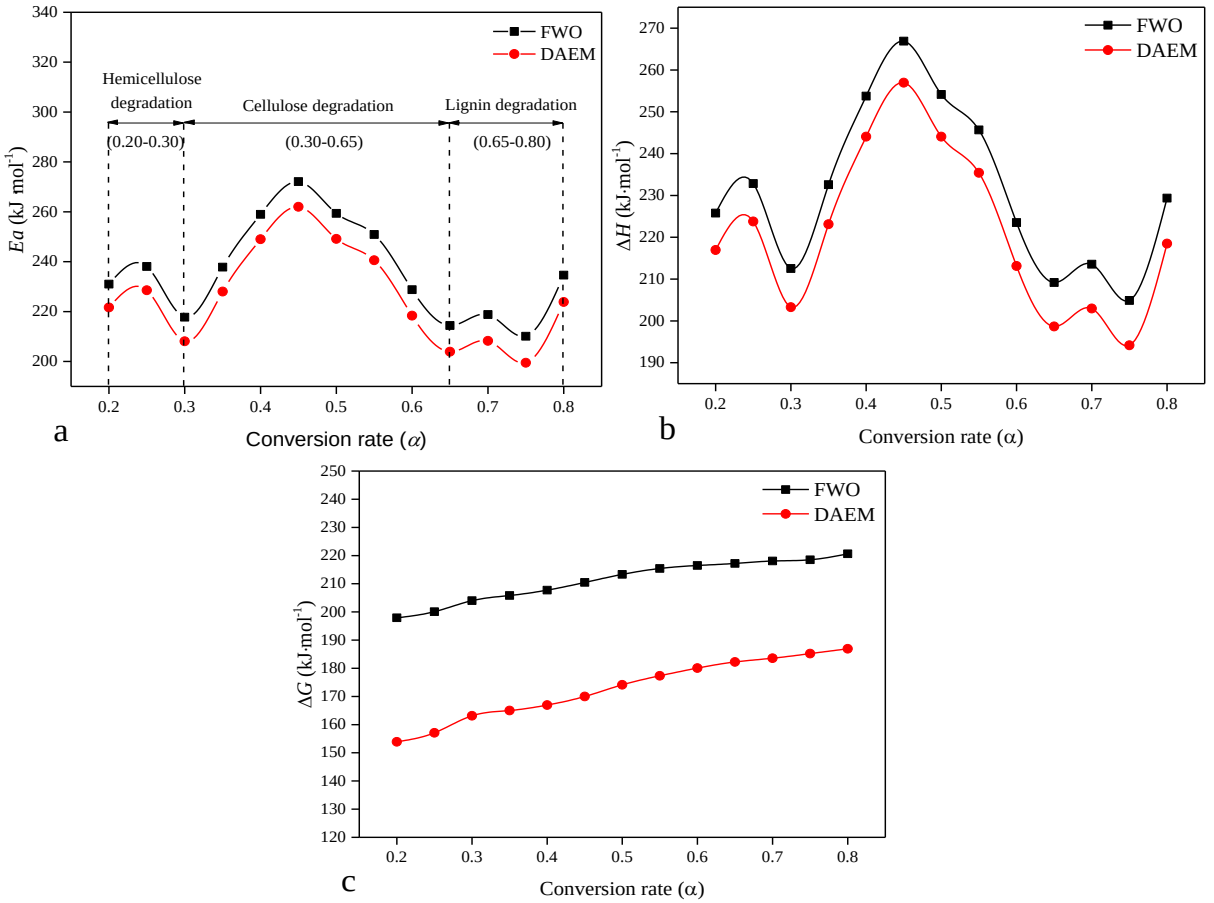

Figure S5. The plots of *Ea* (a), Δ*H* (b), and Δ*G* (c) values as a function of the conversion rate (α) of the SCR pyrolysis.

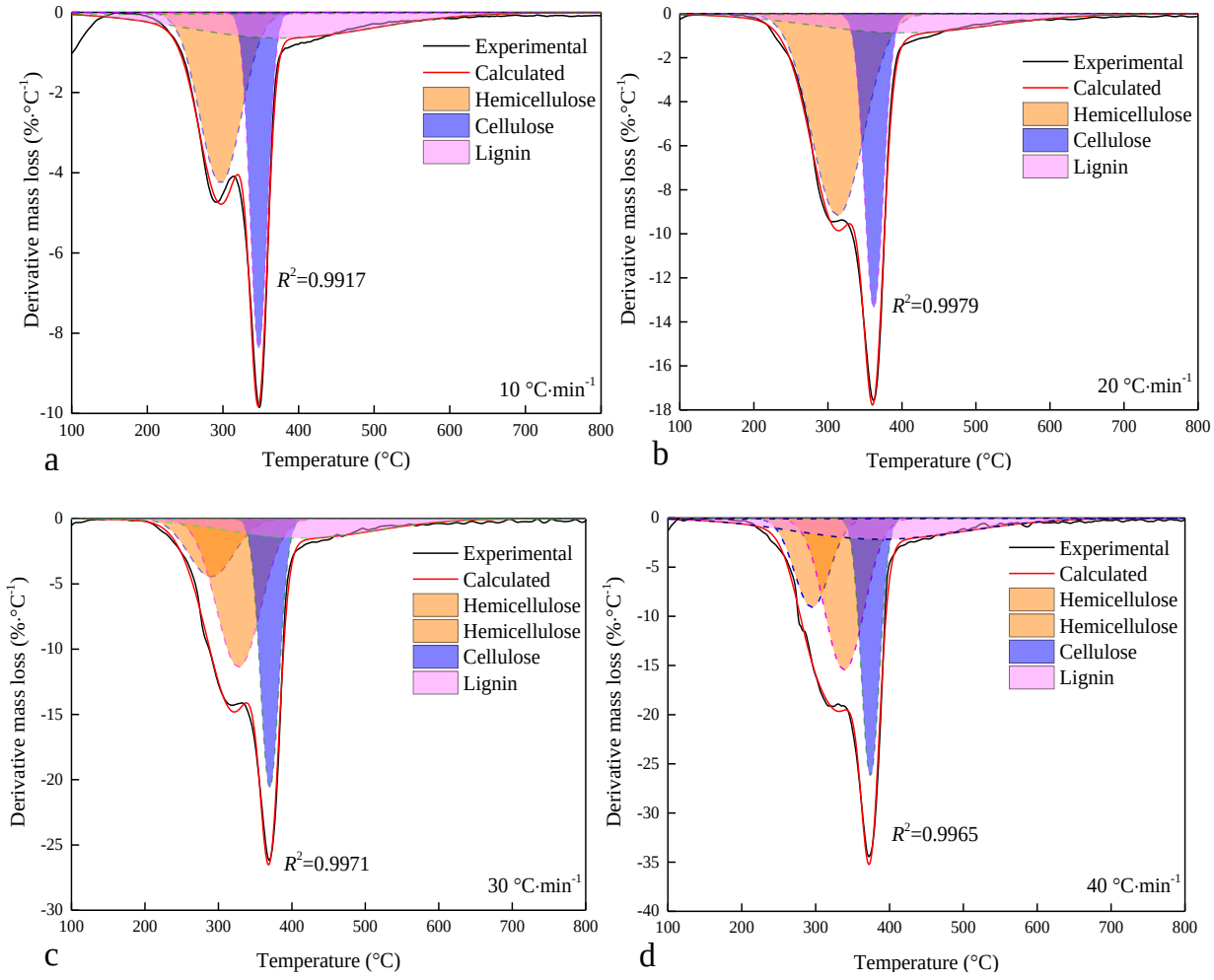

Figure S6. Optimized decomposition process of hemicellulose, cellulose, and lignin pseudocomponents in the SCR at four heating rates.

309

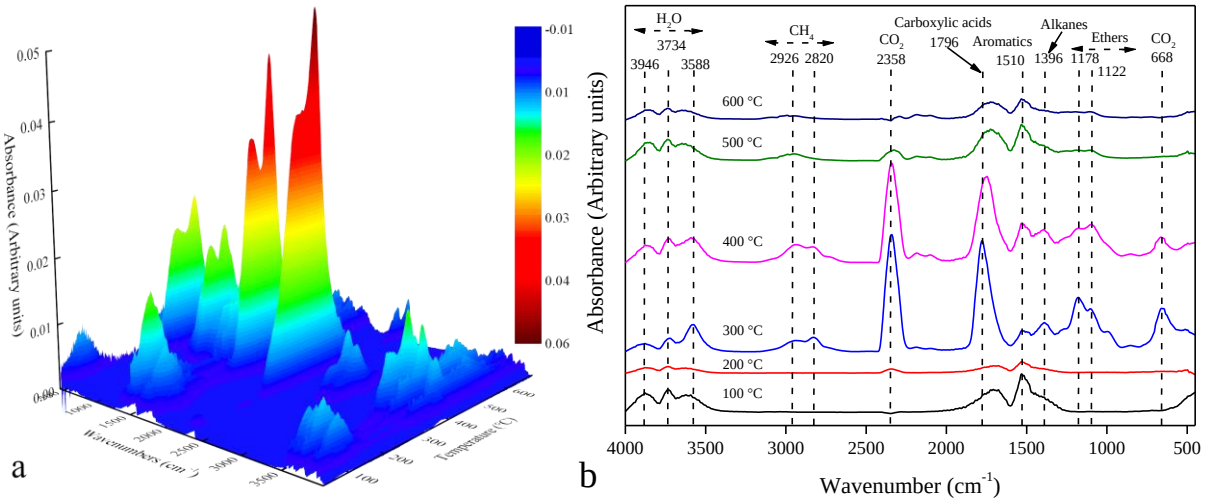

310

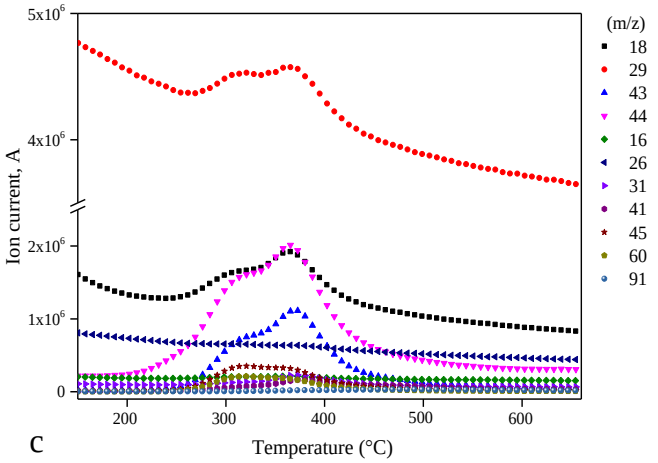

311 **Figure S7.** The 3D FTIR spectrum (a), FTIR spectra at selected pyrolysis temperatures (b) and
312 temperature-dependent curves of the primary MS ionized fragments (c) for the primary analysis
313 of gas products from the SCR pyrolysis.

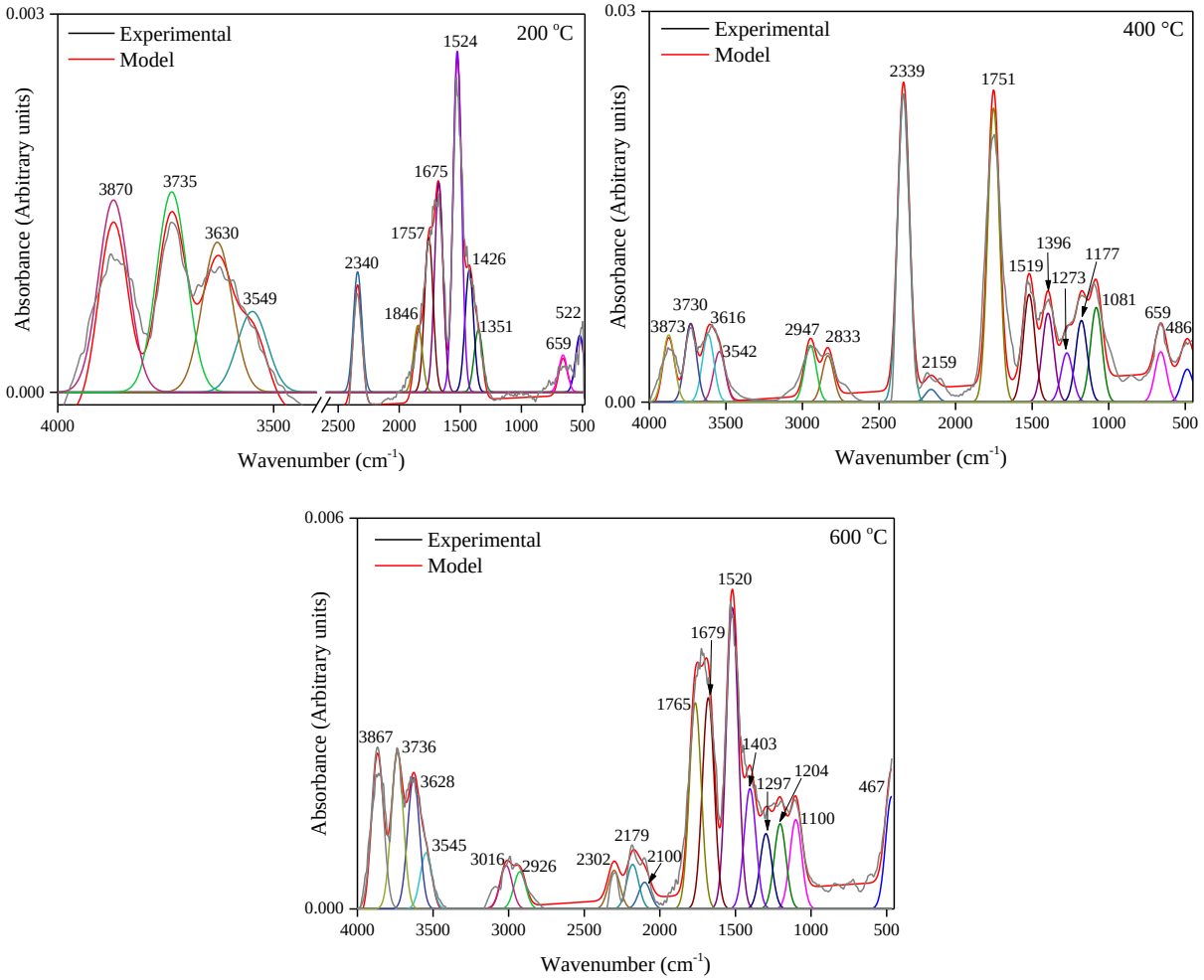

Figure S8. Curve fitting of the TG-FTIR spectra at the selected temperatures of 200, 400, and 600 ℃ for the analysis of gases.

Tables

Table S1. Structural parameters derived from the quantitative ^{13}C NMR spectroscopy.

Alkyl C[a] (%)	Aryl C[a] (%)	Carbonyl C[a] (%)	O-aryl[a] (%)	Non-protonated aromatic C[a] (%)
68.46	28.33	3.22	3.65	10.10
Protonated aromatic C[a] (%)	**$r_{npary/pary}$**	**Aromaticity[b]**	**Aliphatic C[c] (%)**	**Total polar C[d] (%)**
14.58	0.69	29.27	83.04	73.94

[a]Alkyl carbon (C): the sum of alkyl C and O-alkyl C (0–90 ppm); Aryl C: the sum of aryl C and O-aryl C (90–167 ppm); Protonated aromatic C (90–110 ppm); Non-protonated aromatic C (110–148 ppm); O-aryl: oxygenated aromatic C (148–167 ppm); Carbonyl C: the sum of COO/NC=O (167–184 ppm) and C=O groups (184–220 ppm).

[b]Aromaticity = 100 ×Aryl C/(Alkyl C+Aryl C).

[c]Aliphatic C region (0–110 ppm).

[d]Total polar C region (45–90 ppm and 148–220 ppm).

Table S2. Theoretical models of pyrolysis reactions with different $f(\alpha)$ and $g(\alpha)$ functions.

Symbols	Mechanisms	$f(\alpha)$	$g(\alpha)$
Diffusion reaction			
D1	One-way transport	$(1/2)\alpha$	α^2
D2	Two-way transport (Valensi model)	$[-\ln(1-\alpha)]^{-1}$	$\alpha+(1-\alpha)\ln(1-\alpha)$
D3	Three-way transport (Jander model)	$(3/2)(1-\alpha)^{2/3}[1-(1-\alpha)^{1/3}]^{-1}$	$[1-(1-\alpha)^{1/3}]^2$
Zh	Zhuravlev equation	$(2/3)(1-\alpha)^{5/3}/[1-(1-\alpha)^{1/3}]$	$[(1-\alpha)^{-1/3}-1]^2$
GB	Ginstling-Brounshtein equation	$(2/3)(1-\alpha)^{1/3}/[1-(1-\alpha)^{1/3}]$	$1-2\alpha/3-(1-\alpha)^{2/3}$
Chemical reaction			
F1	Sigmoidal rate equations Prout-Tomkins	$\alpha(1-\alpha)$	$-\ln(1-\alpha)$
Power low			
P2	Power low	$2\alpha^{1/2}$	$\alpha^{1/2}$
Order-based reaction			
R2	2^{nd} order random nucleation having two nuclei on individual particle	$(1-\alpha)^2$	$(1-\alpha)^{-1}-1$

Table S3. Thermodynamic parameters of the SCR pyrolysis derived from the FWO and DAEM methods at different conversion rates.

Method	α	Linear equation	Ea (kJ·mol^{-1})	A (s^{-1})	Adj. R^2	ΔH (kJ·mol^{-1})	ΔG (kJ·mol^{-1})	ΔS (J·mol^{-1}·K^{-1})
FWO	0.20	Ln (β) = -27786(1/T) + 52.35	231.02	7.24×10^{15}	0.9882	225.78	197.90	44.16
	0.25	Ln (β) = -28634(1/T) + 53.05	238.08	1.84×10^{16}	0.9885	232.83	200.07	51.90
	0.30	Ln (β) =-26191(1/T) + 48.13	217.77	1.80×10^{14}	0.9971	212.52	204.02	13.46
	0.35	Ln (β) =-28604(1/T) + 51.50	237.83	5.86×10^{15}	0.9951	232.58	205.83	42.39
	0.40	Ln (β) = -31149(1/T) + 55.08	258.99	2.29×10^{17}	0.9891	253.74	207.75	72.86
	0.45	Ln (β) = -32728(1/T) + 56.96	272.12	9.95×10^{19}	0.9629	266.88	210.49	89.34
	0.50	Ln (β) = -31197(1/T) + 53.79	259.39	8.50×10^{16}	0.9850	254.14	213.34	64.64
	0.55	Ln (β) = -30177(1/T) + 51.60	250.91	1.14×10^{16}	0.9942	245.66	215.43	47.90
	0.60	Ln (β) = -27515(1/T) + 46.95	228.77	1.37×10^{14}	0.9790	223.52	216.48	11.16
	0.65	Ln (β) = -25790(1/T) + 43.88	214.43	7.75×10^{12}	0.9903	209.19	217.21	-12.72
	0.70	Ln (β) = -26317(1/T) + 44.44	218.81	1.52×10^{13}	0.9933	213.56	218.07	-7.14
	0.75	Ln (β) = -25272(1/T) + 42.52	210.13	2.67×10^{12}	0.9914	204.88	218.50	-21.58
	0.80	Ln (β) = -28215(1/T) + 46.73	234.60	1.88×10^{14}	0.9869	229.35	220.64	13.80
DAEM	0.20	Ln (β/T^2) = -26659(1/T) + 37.68	221.64	5.31×10^{18}	0.9872	216.95	153.90	99.89
	0.25	Ln (β/T^2) = -27490(1/T) + 38.35	228.55	1.08×10^{19}	0.9875	223.78	157.10	105.65
	0.30	Ln (β/T^2) = -25031(1/T) + 33.40	208.11	6.91×10^{16}	0.9968	203.27	163.15	63.56
	0.35	Ln (β/T^2) = -27425(1/T) + 36.75	228.01	2.15×10^{18}	0.9947	223.10	165.02	92.02
	0.40	Ln (β/T^2) = -29953(1/T) + 40.30	249.03	8.19×10^{19}	0.9882	244.04	166.94	122.17
	0.45	Ln (β/T^2) = -31515(1/T) + 42.14	262.02	5.45×10^{20}	0.9600	256.97	169.98	137.82
	0.50	Ln (β/T^2) = -29968(1/T) + 38.95	249.15	2.13×10^{19}	0.9838	244.04	174.13	110.76
	0.55	Ln (β/T^2) = -28935(1/T) + 36.74	240.57	2.26×10^{18}	0.9937	235.40	177.32	92.01
	0.60	Ln (β/T^2) = -26263(1/T) + 32.08	218.35	1.93×10^{16}	0.9770	213.14	180.09	52.36
	0.65	Ln (β/T^2) = -24529(1/T) + 28.99	203.94	8.23×10^{14}	0.9893	198.68	182.23	26.06
	0.70	Ln (β/T^2) = -25048(1/T) + 29.53	208.25	1.45×10^{15}	0.9926	202.95	183.59	30.69
	0.75	Ln (β/T^2) = -23994(1/T) + 27.60	199.49	2.00×10^{14}	0.9905	194.16	185.20	14.20
	0.80	Ln (β/T^2) = -26925(1/T) + 31.79	223.86	1.50×10^{16}	0.9856	218.48	186.94	49.98

Table S4. Optimized decomposition parameters of SCR pyrolysis at different heating rates.

Heating rates	Pseudocomponents	A_i (%)	T_p (℃)	C_i	r_i (%·℃$^{-1}$)
10 °C·min^{-1}	hemicellulose	40.15	296.96	0.38	0.61
	cellulose	32.80	347.47	0.31	1.27
	lignin	27.05	375.08	0.26	0.14
20 °C·min^{-1}	hemicellulose	53.53	313.31	0.50	0.59
	cellulose	28.90	362.06	0.27	1.11
	lignin	17.57	400.82	0.17	0.09
30 °C·min^{-1}	hemicellulose	15.26	290.17	0.14	0.43
	hemicellulose	38.20	327.66	0.36	0.58
	cellulose	29.60	370.04	0.28	1.08
	lignin	16.94	413.08	0.16	0.09
40 °C·min^{-1}	hemicellulose	17.84	294.98	0.17	0.45
	hemicellulose	34.25	338.91	0.32	0.59
	cellulose	26.88	374.22	0.25	1.07
	lignin	21.03	387.33	0.20	0.68

Table S5. Typical absorption peaks and their corresponding volatile gaseous species determined using TG-FTIR analysis.

Wavenumber range (cm^{-1})	Functional groups	Possible species
3923–3542	O-H stretching	H_2O
3016–2820	C-H stretching	CH_4
2360–2302	C=O stretching	CO_2
2179–2100	C-O stretching	CO
1846–1715	C-O stretching	Carboxylic acids, ketones
1679–1647	C=O stretching	Unconjugated C=O groups
1524–1510	C-C stretching, benzene skeletal	Aromatics
1426–1349	C-H blending	Alkanes
1297–1273	O-H stretching	Phenols
1204–1122	C-O stretching O-H stretching	Ethers
1100–992	O-H stretching C-O(H) stretching	Alcohols
668–467	C=O stretching	CO_2

335 **Table S6.** Primary MS ion fragments and their corresponding possible volatile gaseous species.

No.	m/z	Volatile species	No.	m/z	Volatile species
1	16	CH_4	7	43	Acetaldehyde
2	18	H_2O	8	44	CO_2
3	26	C_2H_2 (acetylene)	9	45	Formic acid
4	29	Aldehydes	10	60	Acetic acid/propanol/ glycol aldehyde/methyl formate
5	31	Alcohols	11	91	Benzenes
6	41	C_3H_6 (propane)			

336

Table S7. The 2D-TG-FTIR-COS results on the assignments and signs of peaks in synchronous and asynchronous (in the brackets) maps for gas products from SCR pyrolysis.

Position *v*2 (cm^{-1})	Assignments	Position *v*1 (cm^{-1}) and signs								
		1142	1522	1736	1770	1794	2336	2942	3744	3828
492	CO_2						(–)			
542	CO_2									–
654	CO_2		(+)	(+)					(+)	
670	CO_2				+		+			
1080	Alcohols					(–)				
1092	Alcohols						(–)			
1142	Ethers	+								
1154	Ethers						+			
1170	Ethers		(+)	(+)	+				(+)	
1715	Carboxylic acids, ketones						(–)			
1736	Carboxylic acids, ketones					(–)				
1764	Carboxylic acids, ketones						+			
1770	Carboxylic acids, ketones				+					
1792	Carboxylic acids, ketones							(+)		
2146	CO						(–)			
2336	CO_2						+			
2340	CO_2									–
2346	CO_2							(+)		

Note: Signs were obtained in synchronous and asynchronous maps from 2D-TG-FTIR-COS analysis. The "+" represents red and positive sign, and the "–" represents blue and negative sign.

References

(1) Song, F.; Wang, X.; Li, T.; Zhang, J.; Bai, Y.; Xing, B.; Giesy, J. P.; Wu, F., Spectroscopic analyses combined with Gaussian and Coats-Redfern models to investigate the characteristics and pyrolysis kinetics of sugarcane residue-derived biochars. *J. Clean. Prod.* **2019,** *237*, 117855.

(2) Pan, L.; Dai, F.; Li, G.; Liu, S., A TGA/DTA-MS investigation to the influence of process conditions on the pyrolysis of Jimsar oil shale. *Energy* **2015,** *86*, 749-757.

(3) He, Q.; Ding, L.; Gong, Y.; Li, W.; Wei, J.; Yu, G., Effect of torrefaction on pinewood pyrolysis kinetics and thermal behavior using thermogravimetric analysis. *Bioresour. Technol.* **2019,** *280*, 104-111.

(4) Miura, K.; Maki, T., A simple method for estimating f(E) and k0(E) in the distributed activation energy model. *Energy Fuels* **1998,** *12*, (5), 864-869.

(5) Mabuda, A. I.; Mamphweli, N. S.; Meyer, E. L., Model free kinetic analysis of biomass/sorbent blends for gasification purposes. *Renew. Sustain. Energy Rev.* **2016,** *53*, 1656-1664.

(6) Ma, Z.; Wang, J.; Zhou, H.; Zhang, Y.; Yang, Y.; Liu, X.; Ye, J.; Chen, D.; Wang, S., Relationship of thermal degradation behavior and chemical structure of lignin isolated from palm kernel shell under different process severities. *Fuel Process. Technol.* **2018,** *181*, 142-156.

(7) Sriram, A.; Swaminathan, G., Pyrolysis of Musa balbisiana flower petal using thermogravimetric studies. *Bioresour. Technol.* **2018,** *265*, 236-246.

(8) Xu, Y.; Chen, B., Investigation of thermodynamic parameters in the pyrolysis conversion of biomass and manure to biochars using thermogravimetric analysis. *Bioresour. Technol.* **2013,** *146*, 485-493.

(9) Singh, B.; Fang, Y.; Cowie, B. C. C.; Thomsen, L., NEXAFS and XPS characterisation of carbon functional groups of fresh and aged biochars. *Org. Geochem.* **2014,** *77*, (22), 1-10.

(10) Song, F.; Wu, F.; Xing, B.; Li, T.; Feng, W.; Giesy, J. P.; Guo, W.; Wang, H.; Liu, S.; Bai, Y., Protonation-dependent heterogeneity in fluorescent binding sites in sub-fractions of fulvic acid using principle component analysis and two-dimensional correlation spectroscopy. *Sci. Total Environ.* **2018,** *616-617*, 1279-1287.

(11) Noda, I., Two-dimensional infrared (2D IR) spectroscopy: Theory and applications. *Appl. Spectrosc.* **1990,** *44*, (44), 550-561.

(12) Chen, W.; Qian, C.; Liu, X.-Y.; Yu, H.-Q., Two-dimensional correlation spectroscopic analysis on the interaction between humic acids and TiO_2 nanoparticles. *Environ. Sci. Technol.* **2014,** *48*, (19), 11119-11126.

(13) Noda, I.; Ozaki, Y., *Chapter 4. Generalized Two-Dimensional Correlation Spectroscopy in Practice*. 2009; 47-64.

(14) Chen, W.; Habibul, N.; Liu, X. Y.; Sheng, G. P.; Yu, H. Q., FTIR and synchronous fluorescence heterospectral two-dimensional correlation analyses on the binding characteristics of copper onto dissolved organic matter. *Environ. Sci. Technol.* **2015,** *49*, (4), 2052-2058.

(15) Zhang, P.; Sun, H.; Yu, L.; Sun, T., Adsorption and catalytic hydrolysis of carbaryl and atrazine on pig manure-derived biochars: Impact of structural properties of biochars. *J. Hazard. Mater.* **2013,** *244-245*, 217-224.

(16) Jin, J.; Li, Y.; Zhang, J.; Wu, S.; Cao, Y.; Liang, P.; Zhang, J.; Wong, M. H.; Wang, M.; Shan, S., Influence of pyrolysis temperature on properties and environmental safety of heavy metals in biochars derived from municipal sewage sludge. *J. Hazard. Mater.* **2016,** *320*, 417-426.

(17) Nogueira, M. C. J. A.; Tavares, M. I. B.; Nogueira, J. D. S., ^{13}C NMR Molecular dynamic investigation of tropical wood Angelin Pedra (Hymenolobium paetrum). *Polymer* **2004,** *45*, (4), 1217-1222.

(18) Sun, K.; Keiluweit, M.; Kleber, M.; Pan, Z.; Xing, B., Sorption of fluorinated herbicides to plant biomass-derived biochars as a function of molecular structure. *Bioresour. Technol.* **2011,** *102*, (21), 9897-9903.

(19) Cao, X.; Pignatello, J. J.; Li, Y.; Lattao, C.; Chappell, M. A.; Chen, N.; Miller, L. F.; Mao, J., Characterization of wood chars produced at different temperatures using advanced solid-state ^{13}C NMR spectroscopic techniques. *Energy Fuels* **2012,** *26*, (26), 5983-5991.

(20) Brewer, C. E.; Schmidt‐Rohr, K.; Satrio, J. A.; Brown, R. C., Characterization of biochar from fast pyrolysis and gasification systems. *Environ. Prog. Sustain. Energy* **2010,** *28*, (3), 386-396.

(21) Chen, D.; Zhou, J.; Zhang, Q., Effects of heating rate on slow pyrolysis behavior, kinetic parameters and products properties of moso bamboo. *Bioresour. Technol.* **2014,** *169*, 313-319.

(22) Liang, F.; Wang, R.; Xiang, H.; Yang, X.; Zhang, T.; Hu, W.; Mi, B.; Liu, Z., Investigating pyrolysis characteristics of moso bamboo through TG-FTIR and Py-GC/MS. *Bioresour. Technol.* **2018,** *256*, 53-60.

(23) Ma, Z.; Chen, D.; Jie, G.; Bao, B.; Zhang, Q., Determination of pyrolysis characteristics and kinetics of palm kernel shell using TGA–FTIR and model-free integral methods. *Energy Convers. Manag.* **2015,** *89*, 251-259.

(24) Angın, D., Effect of pyrolysis temperature and heating rate on biochar obtained from pyrolysis of safflower seed press cake. *Bioresour. Technol.* **2013,** *128*, 593-597.

(25) Yustiawati; Kihara, Y.; Sazawa, K.; Kuramitz, H.; Kurasaki, M.; Saito, T.; Hosokawa, T.; Syawal, M. S.; Wulandari, L.; Hendri, I.; Tanaka, S., Effects of peat fires on the characteristics of humic acid extracted from peat soil in Central Kalimantan, Indonesia. *Environ. Sci. Pollut. Res.* **2015,** *22*, (4), 2384-2395.

(26) Sazawa, K.; Yoshida, H.; Okusu, K.; Hata, N.; Kuramitz, H., Effects of forest fire on the properties of soil and humic substances extracted from forest soil in Gunma, Japan. *Environ. Sci. Pollut. Res.* **2018,** *25*, (30), 30325-30338.

(27) Broido, A.; Nelson, M. A., Char yield on pyrolysis of cellulose. *Combust. Flame* **1975,** *24*, 263-268.

(28) Yang, H.; Yan, R.; Chin, T.; Liang, D. T.; Chen, H.; Zheng, C., Thermogravimetric analysis−Fourier transform infrared analysis of palm oil waste pyrolysis. *Energy Fuels* **2004,** *18*, (6), 1814-1821.

(29) Mallick, D.; Poddar, M. K.; Mahanta, P.; Moholkar, V. S., Discernment of synergism in pyrolysis of biomass blends using thermogravimetric analysis. *Bioresour. Technol.* **2018,** *261*, 294-305.

(30) Mehmood, M. A.; Ye, G.; Luo, H.; Liu, C.; Malik, S.; Afzal, I.; Xu, J.; Ahmad, M. S., Pyrolysis and kinetic analyses of Camel grass (Cymbopogon schoenanthus) for bioenergy. *Bioresour. Technol.* **2017,** *228*, 18-24.

(31) Ahmad, M. S.; Mehmood, M. A.; Al Ayed, O. S.; Ye, G.; Luo, H.; Ibrahim, M.; Rashid, U.; Arbi Nehdi, I.; Qadir, G., Kinetic analyses and pyrolytic behavior of Para grass (Urochloa mutica) for its bioenergy potential. *Bioresour. Technol.* **2017,** *224*, 708-713.

(32) Özsin, G.; Pütün, A. E., Kinetics and evolved gas analysis for pyrolysis of food processing wastes using TGA/MS/FT-IR. *Waste Manag.* **2017,** *64*, 315-326.

(33) Părpăriţă, E.; Nistor, M. T.; Popescu, M.-C.; Vasile, C., TG/FT–IR/MS study on thermal decomposition of polypropylene/biomass composites. *Polym. Degrad. Stabil.* **2014,** *109*, 13-20.

(34) Liu, Q.; Wang, S.; Zheng, Y.; Luo, Z.; Cen, K., Mechanism study of wood lignin pyrolysis by using TG–FTIR analysis. *J. Anal. Appl. Pyrolysis* **2008,** *82*, (1), 170-177.

(35) Wang, S.; Lin, H.; Ru, B.; Sun, W.; Wang, Y.; Luo, Z., Comparison of the pyrolysis behavior of pyrolytic lignin and milled wood lignin by using TG–FTIR analysis. *J. Anal. Appl. Pyrolysis* **2014,** *108*, 78-85.

(36) Kai, X.; Li, R.; Yang, T.; Shen, S.; Ji, Q.; Zhang, T., Study on the co-pyrolysis of rice straw and high density polyethylene blends using TG-FTIR-MS. *Energy Convers. Manag.* **2017,** *146*, 20-33.

(37) Singh, S.; Wu, C.; Williams, P. T., Pyrolysis of waste materials using TGA-MS and TGA-FTIR as complementary characterisation techniques. *J. Anal. Appl. Pyrolysis* **2012,** *94*, 99-107.

(38) Kai, X.; Yang, T.; Shen, S.; Li, R., TG-FTIR-MS study of synergistic effects during co-pyrolysis of corn stalk and high-density polyethylene (HDPE). *Energy Convers. Manag.* **2019,** *181*, 202-213.